Explaining monthly precipitation anomalies in northwestern South America by integrating vertical dynamics and energetics

Jose Obregon-Yataco[1]

[1]Ciencias de la Atmósfera, Hidrósfera y Cambio Climático, Instituto Geofísico del Perú, Lima, Peru

Correspondence: Jose Obregon-Yataco (jobregyat@gmail.com)

Abstract. Northwestern South America (NWSA) is a critical region for monitoring El Niño-driven hydroclimatic extremes, receiving its maximum cumulative precipitation in March. Thermodynamic indices alone often fail to explain observed precipitation anomalies in this region because they neglect the limiting role of large-scale environmental dynamics. To bridge this gap, a diagnostic proxy called the Buoyancy Work Rate (BWR) is proposed, which quantifies the rate of conversion from potential to kinetic energy by coupling local thermodynamic instability (ΔT) with vertical motion (ω) forced by large-scale dynamics. The BWR is calculated by vertically integrating the product $-\omega\Delta T$ from the surface to the 100 hPa level. Using the PCMCI+ causal discovery algorithm, this study empirically validates the classical thermodynamic energy balance mechanism, demonstrating that precipitation in the NWSA is dynamically controlled, with ω exerting a causal influence significantly stronger than local evaporation. Validation via Tail Dependence analysis (λ_U) reveals that the BWR achieves robust asymptotic dependence ($\lambda_U \approx 0.8$) during extreme events, effectively filtering out thermodynamic false positives (e.g., the 2016 event) by incorporating the vertical velocity constraint. Furthermore, autocorrelation analysis indicates that the inclusion of the thermodynamic component imparts significant signal persistence to the index, stabilizing the inherently chaotic nature of pure vertical velocity. Physically, the index explains how dynamic forcing modulates precipitation outcomes across events with similar instability, resolving the contrasting impacts of the 2016, 2017, and 2023 El Niño events. Consequently, the BWR emerges as a physically consistent tool that offers a longer predictability horizon for monitoring sub-seasonal hydroclimatic risks.

1 Introduction

The El Niño-Southern Oscillation (ENSO) is one of the main drivers of global climate variability, altering weather patterns worldwide (McPhaden et al., 2006; Wang et al., 2016). Northwest South America (NWSA) is a region of critical scientific importance for monitoring these events, particularly coastal El Niño events, while being exceptionally vulnerable to their hydroclimatic and socioeconomic impacts (Callahan and Mankin, 2023; Poveda et al., 2025).

Although sea surface temperature (SST) in the Niño 1+2 region possesses a known critical threshold capable of triggering deep convection (Takahashi and Martínez, 2017; Takahashi et al., 2018), SST alone has proven to be an insufficient predictor of precipitation anomalies (Sulca and Takahashi, 2025). It has been demonstrated that above a certain SST threshold (approximately 28 °C), the direct relationship between local temperature and convection breaks down, with convective activity

becoming increasingly controlled by large-scale vertical motions rather than surface fluxes alone (Lau et al., 1997; Bony et al., 1997).

Estimating precipitation anomalies remains a significant challenge, as it requires understanding deep moist convection, the process of vertical heat and moisture transport driving tropical climates (Houze, 2004). This process is governed by a complex interaction between local thermodynamic instability and large-scale atmospheric dynamics. For decades, the conventional metric for assessing this potential has been Convective Available Potential Energy (CAPE) (Emanuel, 1994). However, purely thermodynamic indices often yield high false-positive rates in the tropics because they quantify potential instability without accounting for the dynamic forcing required to release it (Williams and Renno, 1993; DeMott and Randall, 2004). Conversely, large-scale vertical motion (ω) explains a significantly larger fraction of variance in tropical convection than local SST (Lau et al., 1997). This dynamic dominance was physically grounded by **?**, who demonstrated that on climatic timescales within the Walker circulation, latent heat release is primarily balanced by adiabatic cooling due to vertical ascent ($[\theta]_z \omega \approx Q$). This balance implies that rainfall is dynamically maintained by moisture convergence rather than locally fueled by surface evaporation, necessitating indices that explicitly incorporate vertical velocity.

This disconnect between thermodynamic potential and realized convection is particularly evident in the Eastern Pacific. The 2017 and 2023 Coastal El Niño events produced extreme rainfall, whereas the 2015-2016 global El Niño, despite comparable SST magnitudes, did not produce equally severe coastal impacts (Paek et al., 2017; Sulca et al., 2017). To distinguish these regimes, indices such as the C and E indices (Takahashi et al., 2011) and the atmospheric $CPTICZ$ and $EPTICZ$ indices (Sulca and Takahashi, 2025) were developed. However, a unified metric linking the thermodynamic potential with the dynamic realization of convection on monthly scales remains necessary.

While atmospheric dynamics occur on high-frequency timescales (Zipser, 2003), this study focuses on monthly averages to isolate robust climate signals (Trenberth, 1997). Based on the thermodynamic energy balance described by **?**, the monthly average vertical motion serves as a robust proxy for the integrated heating of the column. Consequently, the main objective of this research was to develop, validate, and apply the Buoyancy Work Rate (BWR) index. The BWR is defined as the vertical integration of the product of vertical velocity (ω) and parcel buoyancy (ΔT). It should be noted that while the BWR does not carry strict units of power density (W m^{-2}), it serves as a physical proxy proportional to the rate at which buoyancy potential energy is converted into kinetic energy. By coupling the dynamic trigger (ω) with the thermodynamic fuel (ΔT), the BWR is designed to distinguish buoyancy-driven convection from mechanically forced vertical motion (where $\Delta T < 0$), providing a diagnostic of active, thermodynamically supported deep convection.

In this study, the performance of the BWR was rigorously evaluated against precipitation anomalies in the NWSA from 1981 to 2025. First, Causal Discovery algorithms, specifically PCMCI+ (**?**), were applied to verify the physical hypothesis that dynamics drive precipitation more strongly than local evaporation, validating the mechanism proposed by **?**. Second, the reliability of the index during extreme events was assessed using the Upper Tail Dependence Coefficient (λ_U) derived from Copula theory (**?**), determining whether the BWR maintains its coupling with precipitation during the most intense El Niño events. Finally, the predictability horizon of the index was analyzed via autocorrelation functions to determine if the inclusion of the thermodynamic component (ΔT) imparts greater signal persistence compared to pure vertical velocity.

2 Data and study area

2.1 Observational and Reanalysis Data

Monthly mean air temperature (T_a), relative humidity (RH), and zonal, meridional, and vertical wind components were obtained from the ERA5 reanalysis dataset (Hersbach et al., 2020). These data were utilized for the period 1981–2025 across 27 vertical pressure levels ranging from 1000 to 100 hPa, with a spatial resolution of 0.25°.

To validate the proposed climate index, two independent high-resolution precipitation products developed specifically for the complex Peruvian topography were employed. First, the RAIN4PE product (Fernandez-Palomino et al., 2022) was used for the 1981–2015 period. RAIN4PE is a gridded dataset that merges three data sources–satellite estimates (CHIRPS), reanalysis data (ERA5), and ground observations-corrected via quantile mapping and validated through hydrological modeling to ensure consistency with observed streamflow and water balance closure. Second, the PISCO product (Peruvian Interpolated Data of the SENAMHI's Climatological and Hydrological Observations) (Aybar et al., 2019) was used for the 1981–2025 period. PISCO is a hybrid product developed by the National Meteorology and Hydrology Service of Peru (SENAMHI) that combines quality-controlled rain gauge records with satellite covariates (CHIRPS) using geostatistical interpolation techniques to reconstruct rainfall fields over data-scarce regions.

It is important to note that the stable version of PISCO, which incorporates both manual and automatic quality control (Aybar et al., 2019), is available only for the 1981-2016 period; consequently, the unstable version, which undergoes only automatic quality control, was utilized for the 2017-2025 period. Due to RAIN4PE only having data until 2015 and the uncertainty of PISCO increasing from 2017 onwards, monthly precipitation from ERA5 (Hersbach et al., 2020), was used to evaluate similarities among the precipitation products as a form of data triangulation to increase the credibility of precipitation anomaly behavior. Fig. 2 shows that ERA5 is correlated significantly over all the domain with RAIN4PE and PISCO, being more strong near to the coast between Peru and Ecuador. Finally, monthly sea surface temperature (SST) was also utilized to provide context for the identified rainiest and driest events.

2.2 Study area: The NWSA and the coastal coupling zone

Two domains of interest were defined: the broader NWSA region (18.95° S–1.95° N, 81.95° W–67.05° W) and a specific coastal subdomain adjacent to the Niño 1+2 region (81.25° W–78.5° W, 8° S–0.75° N) (Fig. A3).

The selection of this coastal subdomain is physically motivated by the energy balance framework proposed by **?**. This area typically lies beneath the descending branch of the Walker circulation, characterized by strong subsidence and thermal inversion that suppresses convection. Consequently, it serves as an ideal natural laboratory to verify the hypothesis that precipitation anomalies are driven by the dynamic interruption of this subsidence (adiabatic cooling via vertical motion, ω) rather than by local surface evaporation, as the region acts as a boundary zone between stable and unstable regimes.

Figure 1 presents the precipitation climatology (1981–2015) from PISCO averaged over this coastal subdomain. It is observed that March constitute the rainiest month; this seasonal peak represents a critical coupling window where dynamic relax-

ation (weakening of trade winds) and thermodynamic instability (SST warming) come into phase, facilitating the development of deep convection (**???**Peng et al., 2024).

3 Methodology

3.1 Identification of Rainiest and Driest Events as Diagnostic Case Studies

To characterize the distinct vertical atmospheric configurations associated with extreme hydroclimatic anomalies, a set of representative case studies was identified. Monthly precipitation was averaged over the coastal NWSA region adjacent to Niño 1+2 (Fig. A3), and anomalies were calculated from the PISCO dataset relative to the 1981–2015 climatological median. Two arbitrary thresholds were defined solely for event selection purposes: anomalies below -60 mm month^{-1} were used to detect significant dry events, and anomalies above 80 mm month^{-1} were used to detect extreme rainy events. It is important to clarify that these thresholds were applied exclusively to select events for physical diagnosis (e.g., analyzing vertical structure) and were not utilized to calibrate or derive the formulation of the proposed index.

To determine the spatial core of these anomalies, the vertical motion field was analyzed through latitudinal and longitudinal cross-sections. The longitude of 80° W and latitude of 5° S were identified as the axes of maximum vertical ascent over the coastal domain. This geometric characterization allowed for the identification of subsidence and convective layers, as well as the specific pressure levels where convection was initiated and suppressed during the selected case studies.

3.2 Buoyancy Work Rate (BWR) formulation

The formulation of the BWR is physically grounded in the thermodynamic energy balance of the Walker circulation described by **?**, which posits that on climatic timescales, latent heat release (Q) is primarily balanced by adiabatic cooling due to vertical motion ($-\omega \partial\theta/\partial p$). Consequently, an index capable of estimating precipitation must explicitly couple the dynamic trigger (vertical velocity) with the thermodynamic fuel (buoyancy).

First, the dew point temperature (T_d) was calculated from relative humidity following Bolton (1980). Using surface T_d and air temperature (T_a), the parcel temperature path was computed and compared against the environmental temperature profile to yield the parcel buoyancy (ΔT) for every grid point. To construct the index, the product of vertical velocity (ω) and parcel buoyancy (ΔT) was analyzed.

The Buoyancy Work Rate (BWR) is defined as the vertical integration of this product from the surface to 100 hPa with respect to the natural logarithm of pressure ($d\ln P$), as shown in Eq. (1).

$$BWR = -\int_{sfc}^{100} \omega \Delta T \, d\ln P \tag{1}$$

In this integration, only layers exhibiting positive buoyancy ($\Delta T > 0$) and upward motion ($\omega < 0$) were included. This constraint ensures that the index specifically quantifies the rate at which potential energy is converted into kinetic energy during deep convection, filtering out stratiform or forced ascent in stable environments.

It is acknowledged that the BWR serves as a diagnostic proxy proportional to the rate of work performed by buoyancy, rather than a strict physical quantity of energy flux density (W m^{-2}), due to the combination of kinematic and thermodynamic units. However, this hybrid formulation is proposed to capture the non-linear interaction between large-scale dynamics and local instability, which neither variable alone can fully represent.

3.3 Validation framework

To evaluate the physical robustness and predictive utility of the BWR, a multi-tiered validation framework was implemented, moving from causal verification to statistical comparative evaluation.

3.3.1 Causal discovery and physical drivers

To verify the physical hypothesis that large-scale dynamics (ω) exert a stronger control on precipitation than local surface fluxes, the PCMCI+ causal discovery algorithm (**?**) was applied. This method, based on the PC algorithm and Momentary Conditional Independence (MCI) tests, allows for the identification of causal directions and time-lagged links from observational data, filtering out spurious correlations.

The causal analysis was performed using time series of monthly standardized anomalies averaged over land pixels within the NWSA adjacent to Niño 1+2 (81.25° W–78.5° W, 8° S–0.75° N). The variables included in the network were local evaporation, precipitation, and vertical velocity at 500 hPa (ω_{500}). The 500 hPa level was specifically selected because it typically corresponds to the level of maximum vertical mass flux in the tropical troposphere; according to the energy balance framework of **?**, ω at this mid-tropospheric level serves as the most robust proxy for the column-integrated adiabatic cooling required to balance convective latent heat release. Additionally, parcel buoyancy averaged between 700 and 400 hPa ($\Delta T_{700-400}$) and the BWR index were included, with Sea Surface Temperature (SST) averaged over the Niño 1+2 region set as a boundary condition. Contemporaneous links (lag-0) were explicitly permitted in the PCMCI+ setup; this configuration was necessary to capture rapid atmospheric interactions, such as the thermodynamic triggering of convection, that occur on timescales faster than the monthly sampling resolution of the dataset.

3.3.2 Analysis of extremes and predictability

Standard correlation metrics often underestimate performance during extreme events. Therefore, the Upper Tail Dependence Coefficient (λ_U) was calculated using empirical copulas (**?**). Following the methodology of **?**, λ_U was calculated across varying quantile thresholds to assess asymptotic dependence without imposing parametric assumptions. This approach allows for the evaluation of the robustness of the BWR during extreme precipitation events (e.g., strong El Niño years). Furthermore, to evaluate the signal memory and potential predictability horizon of the index compared to its individual components, auto-

correlation functions were computed. For both the tail dependence and autocorrelation analyses, the time series utilized were the monthly standardized anomalies of the BWR, ω_{500}, and $\Delta T_{700-400}$, averaged spatially over the land pixels of the NWSA adjacent to Niño 1+2.

3.3.3 Statistical comparative evaluation with established indices

The diagnostic skill of the BWR was compared with indices previously tested in the region: the Convective Available Potential Energy (CAPE) (Emanuel, 1994) and the Gálvez-Davison Index (GDI) (Gálvez, 2016), both evaluated for the NWSA by Rivas Quispe et al. (2024); and the asymmetric (I_a) and double ITCZ (I_d) indices proposed by Yu and Zhang (2018), assessed by Aliaga-Nestares et al. (2023).

Performance was evaluated using the spatial distribution of the Pearson correlation coefficient (R) and Root Mean Square Error (RMSE) between the indices and three precipitation products (ERA5, PISCO, RAIN4PE) for the 1981–2015 period. Given that the evaluated indices and precipitation products possess disparate physical units and scales (e.g., J kg^{-1} for CAPE versus mm month^{-1} for precipitation), all time series were converted to standardized anomalies prior to the calculation of RMSE and scatterplot generation to ensure comparable magnitudes. Finally, to evaluate performance specifically over the coastal region adjacent to Niño 1+2, indices and precipitation were averaged over land pixels within the domain defined by 81.25° W–78.5° W and 8° S–0.75° N. Scatterplots and time series were analyzed to identify regimes where the BWR offers advantages or limitations compared to purely thermodynamic or precipitation-based indices.

4 Results

4.1 BWR Performance and diagnostic skill

To quantify the skill of the BWR relative to established indices, the spatial distribution of the Pearson correlation coefficient (R) was analyzed (Fig. 3). The BWR and CAPE exhibited the strongest correlations specifically over the NWSA region adjacent to Niño 1+2. However, the performance of CAPE was spatially inconsistent, showing non-significant or even negative correlations over the Amazon. This suggests that while thermodynamic potential is necessary, it is not a sufficient condition for precipitation in continental regimes where dynamic forcing varies independently. The GDI showed significant correlations across the entire domain but with lower magnitudes ($R \leq 0.7$) compared to the BWR in the coastal zone. The indices I_a and I_d (Figs. A1 3) demonstrated the poorest performance, likely due to their reliance on precipitation gradients rather than direct convective physics.

The Root Mean Square Error (RMSE) maps (Fig. A2) further corroborate these findings, with the BWR minimizing error along the coast, although higher errors persist in the eastern Andes, a common challenge for reanalysis-based indices over complex topography.

Focusing on the critical coastal domain (NWSA adjacent to Niño 1+2), the standardized scatterplots (Fig. 4) reveal that the BWR achieves the highest linear association and lowest dispersion among all evaluated indices. Unlike I_a and I_d, which show

little relation to the intensity of anomalies, the BWR scales proportionally with precipitation magnitude without requiring bias correction.

While the BWR calculation requires surface dewpoint temperature (Td), which is strongly coupled to SST boundary conditions, the GDI requires mid-tropospheric humidity, which is highly sensitive to convective parameterization schemes, leading to substantial inter-model spread in the tropics and biases at climatic timescales (**??**). Unlike surface variables, which are well-constrained by oceanic boundary conditions, humidity in the free troposphere exhibits relative biases often exceeding 50-100

The temporal evolution of the indices (Fig. 5) highlights specific strengths. The BWR outperformed other indices in capturing the magnitude of the extreme 1983 and 1998 El Niño events. For the 1998 event, the index aligned closely with precipitation observations, helping to resolve discrepancies between PISCO and RAIN4PE products. In the recent 2023 Coastal El Niño, all indices and ERA5 precipitation peaked in March-April; however, the PISCO product exhibited a sudden and physically unexplained decline in April. Furthermore, during the 2024 dry event, PISCO showed a contradictory positive anomaly peak, whereas BWR, CAPE, and ERA5 precipitation consistently indicated negative anomalies. These discrepancies suggest potential inconsistencies in the automatic quality control of the PISCO dataset for the post-2017 period, reinforcing the value of the BWR as a robust independent diagnostic tool when observational networks are uncertain.

4.2 Causal discovery of precipitation in the NWSA

To determine the primary physical drivers governing precipitation anomalies in the NWSA adjacent to Niño 1+2 on monthly timescales, a causal discovery analysis was conducted using the PCMCI+ algorithm. This approach allows for going beyond statistical correlation to identify directional dependencies and quantify the relative strength of thermodynamic versus dynamic forcing.

Initially, an agnostic approach was adopted, implementing the algorithm without imposing strict structural assumptions regarding the relationships between vertical velocity at 500 hPa (ω_{500}), local evaporation, and precipitation (Fig. 6a). The results reveal a clear hierarchy in the drivers of precipitation. The causal link from ω_{500} to precipitation is the dominant feature of the network [MCI: -0.59], exhibiting a causal strength nearly three times greater than that of local evaporation [MCI: -0.22].

Regarding the surface flux, the negative causal link between evaporation and precipitation must be interpreted in the context of the sign convention, where negative values indicate upward moisture flux. Thus, this relationship implies that positive precipitation anomalies are associated with increasingly negative surface latent heat flux anomalies (i.e., enhanced local evaporation). This behavior is consistent with the seasonal cycle of the NWSA region: unlike the open tropical ocean where deep convection is quasi-permanent and cloud shading can suppress evaporation (negative feedback), the NWSA is largely controlled by large-scale subsidence, with precipitation restricted to the austral summer. Consequently, on an annual basis, periods of higher precipitation coincide with periods of higher surface moisture supply. However, the significantly lower magnitude of the evaporation link compared to ω_{500} confirms that while local surface fluxes provide necessary moisture, they are not the sufficient or primary trigger for convection. Deep convection in this region is fundamentally controlled by the relaxation of large-scale subsidence (dynamic forcing), validating the focus on vertical velocity for the proposed index.

Building upon this established dynamic control, a second causal analysis was performed to evaluate the structural coherence of the proposed Buoyancy Work Rate (BWR) index (Fig. 6b). In this setup, physical link assumptions were introduced to test the dependence of BWR on its constituent components. The resulting causal architecture confirms that parcel buoyancy (ΔT) is causally driven by SST variations [MCI: +0.75], reflecting the thermodynamic preconditioning of the boundary layer by the ocean.

Additionally, the causal influence of SST on local evaporation observed in the network is physically attributable to thermodynamic adjustments. The warming of the ocean surface heats the overlying air, which is subsequently transported via horizontal advection toward the coastal continent. This increase in air temperature induces a decrease in relative humidity, thereby generating a moisture deficit that enhances the upward evaporation flux from the surface to the atmosphere in an attempt to restore thermodynamic equilibrium. Furthermore, ω_{500} and ΔT are identified as independent parents converging on the BWR node. Notably, even when the BWR is introduced into the network, the dynamic signal remains robust, and the BWR index exhibits a causal association with precipitation [MCI: 0.28] that is stronger than the local evaporation signal [MCI: -0.23] in the multi-variable graph. This validates the BWR formulation as a physical integrator that effectively couples the dominant dynamic trigger with the thermodynamic fuel.

4.3 Physical mechanisms during rainiest and driest events

To characterize the atmospheric conditions associated with extreme hydroclimatic anomalies, the March precipitation fields were analyzed (Fig. 2). Based on the thresholds defined in Sect. 3.1, the years 1983, 1993, 1998, 2002, 2017, 2022, 2023 and 2025 were identified as the rainiest events, whereas 1982, 1985, 1988, 2003, 2011 and 2018 were classified as the driest. These extremes are generally associated with coastal El Niño and La Niña phases, as evidenced by the SST anomalies in the Niño 1+2 region (Fig. A4). Specifically, positive SST anomalies characterize the rainiest years, while negative anomalies typically prevail during the driest ones. A notable exception is March 2022, which exhibited cool conditions up to 4° S front the coast, despite being a rainy event. Additionally, the 2016 event was included in the analysis due to the prevailing strong global El Niño conditions, despite its lack of extreme coastal precipitation, to serve as a contrasting case study.

4.3.1 Precipitation spatial distribution in the NWSA

The spatial footprint of the anomalies reveals distinct regimes (Fig. 8) in the NWSA adjacent to Niño 1+2. In the rainiest events, positive anomalies extended across nearly the entire domain, stimulating deep convection (Fig. 8b,e,f,g,k,m,n,o).

However, the 2016 event (Fig. 8j) exhibited a decoupling between global conditions and local impacts, dominated by anomalies ranging from slightly positive to negative. That event had a stronger signal in the Central Pacific (CP) than in the Eastern Pacific (EP), where maximum warming was confined to the Niño 3.4 region rather than the far eastern Pacific (Takahashi et al., 2011). Physically, this configuration shifts the ascending branch of the Walker Circulation westward, forcing a compensatory subsidence limb over the NWSA which inhibits rainfall (Sulca et al., 2017; Paek et al., 2017).

This mechanism was particularly evident in 2016. Sulca et al. (2017) noted that the "atmospheric bridge", which typically teleconnects equatorial warming to the South American coast, was not established. The Intertropical Convergence Zone (ITCZ)

showed limited southward displacement, and the ascending motion remained anchored to the Central Pacific. Consequently, the descending branch of the Walker Circulation did not shift sufficiently eastward to be replaced by ascent over the coast, leaving the region under stable, dry air (Paek et al., 2017). This "out-of-phase" response resulted in moisture deficits, contrasting with the surplus observed during Eastern Pacific events like 1983 or 1998 (Sanabria et al., 2019).

In contrast, the 2017 event was driven by a localized relaxation of the trade winds and sudden coastal warming (approx. 29°C), triggered not by remote Kelvin waves but by atmospheric teleconnections (Rossby wave trains) originating from deep convection in the western Pacific (Echevin et al., 2018; Garreaud, 2018; Aguirre-Correa et al., 2025). This highlights the sensitivity of the region to distinct atmospheric forcing mechanisms.

Regarding the driest events, negative anomalies dominated the domain (Fig. 8a,c,d,h,i,l). These events were associated with coastal La Niña conditions (Fig. A4a,c,d,h,i,l), characterized by enhanced coastal upwelling and cooler-than-average Sea Surface Temperatures (SST) that stabilize the marine boundary layer and suppress convective activity. Specifically, the years 1996, 2007, and 2011 correspond to well-documented periods of significant meteorological drought in the region. **?** identified severe rainfall deficits in the northern Peruvian coast during these years, mechanically linked to the strengthening of the South Pacific Anticyclone and the resulting intensification of the southeasterly trade winds. Furthermore, **?** highlighted that the 2010-2011 La Niña event caused widespread hydrological deficits across the Andean and coastal catchments, severely impacting water availability for agriculture. These dry anomalies are consistent with the suppression of the seasonal southward migration of the ITCZ, which remains north of the equator during La Niña phases, depriving the NWSA of its primary source of deep convection during the austral summer (Sulca et al., 2017).

4.3.2 Cross-section analysis in the NWSA adjacent to Niño 1+2

The vertical structure of the atmosphere reveals a distinct dynamic signature for the rainiest events. Consistent air ascent was observed around 80° W and 5° S in the middle to upper troposphere (Figs. 9 and 10), with the most intense vertical motion occurring during the 1998 El Niño and the 2017 Coastal El Niño. Notably, subsidence was observed in the planetary boundary layer (PBL) for all these rainiest cases. This suggests that the air parcels had to overcome a low-level inhibition barrier to reach the level of free convection, highlighting the necessity of strong dynamic forcing to breach this cap. Conversely, the driest events were characterized by weak ascent near the PBL but dominant subsidence in the middle to upper troposphere around 80° W and 5° S, effectively capping any shallow convection.

The 2016 event provides a critical counter-example. Although weak ascent was present near the PBL around 5° S (Fig. 10j) and 80° W (Fig. 9j), it was overlaid by significant subsidence in the middle troposphere. This mid-level suppression explains the neutralization of potential rainfall despite the favorable large-scale context. In sharp contrast, the 2017 event, which was dynamically uninhibited, produced extreme rainfall in the northern Peruvian departments of Piura, Tumbes, and Lambayeque, exceeding historical records in several locations (**?**Thielen et al., 2023).

4.3.3 Vertical structure analysis

The interaction between thermodynamics and dynamics is quantified in the vertical profiles of ΔT, ω, and the product $-\omega\Delta T$ at the convective core (80° W, 5° S) (Fig. 11). The positive area enclosed by the $-\omega\Delta T$ profile represents the Buoyancy Work Rate (BWR).

For the rainiest events, a consistent pattern of sustained deep tropospheric ascent was observed, aligning with the cross-section analysis. Notably, the 1998 El Niño exhibited the strongest BWR integral, followed by the 2017 Coastal El Niño, which surpassed even the 1983 event in terms of dynamic intensity. Crucially, while the parcel buoyancy (ΔT) values were comparable across 1983, 1998, and 2017, the primary discriminator was the magnitude of the vertical velocity (ω). This implies that the troposphere in 1998 and 2017 provided significantly stronger dynamic forcing than in 1983. Although the 1983 air parcels required less energy to overcome Convective Inhibition (CIN), the resulting BWR was lower due to weaker upward motion. This underscores that warm SSTs (Fig. A4) provide the necessary thermodynamic potential (Takahashi and Martínez, 2017), but the intensity of the event is modulated by the dynamic response (Echevin et al., 2018).

Conversely, the driest events were dynamically characterized by significant mid-level subsidence ($\omega > 0$ around 600 hPa). This suppression is consistent with a strengthened descending branch of the Walker Circulation (**?**) and the stabilizing effect of negative SST anomalies, which enhance the coastal inversion (**?**). Even in the absence of local cooling, teleconnected subsidence from Central Pacific forcing can induce similar drying effects (**?**Sulca et al., 2017).

4.4 Validation of extremes and signal persistence

To rigorously evaluate the robustness of the BWR and its constituent components during critical hydroclimatic phases, a Tail Dependence analysis was conducted using empirical Copulas on the standardized anomalies. This approach allows for the quantification of the conditional probability that precipitation exceeds a high quantile given that the predictor index also exceeds the same quantile, providing a measure of asymptotic dependence essential for risk assessment.

The Upper Tail Dependence Coefficient (λ_U) profiles reveal a clear hierarchy in the physical drivers of extreme precipitation (Fig. 13 and A5). Consistent with the energy balance mechanism described by **?**, vertical velocity at 500 hPa (ω_{500}) exhibits the strongest and most stable asymptotic dependence with precipitation, reaching λ_U values near 0.9 for the highest quantiles (Fig. A5). This confirms that large-scale dynamic ascent is the primary sufficient condition for extreme rainfall events in the NWSA.

The BWR index also demonstrates strong asymptotic dependence, peaking near 0.8 at the 97.5th percentile (Fig. 13). However, a slight decrease in performance is observed in the extreme tail compared to pure ω_{500}. To understand this divergence, the thermodynamic component (ΔT, averaged 700–400 hPa) was analyzed independently (Fig. A6). It was found that ΔT exhibits asymptotic independence (λ_U decreases as quantiles increase), implying that extreme parcel buoyancy does not linearly translate to extreme precipitation without dynamic support. Consequently, the thermodynamic term acts as a slight dampening factor on the BWR at the most extreme percentiles, likely reflecting cases where dynamic forcing is strong enough to drive heavy rainfall even in environments of moderate thermodynamic instability.

The copula space visualization (Fig. 13, left) exhibits a cross-like structure. While the main diagonal confirms the primary physical coupling (positive correlation), the anti-diagonal reveals the presence of regime mismatches in moderate conditions (e.g., dry ascent or false positives). However, the Upper Tail Dependence Coefficient (λ_U) analysis (Fig. 13, right) demonstrates that this noise fades in the extremes. The λ_U coefficient actually increases for higher quantiles, peaking near 0.8 at the 97.5th percentile. This confirms asymptotic tail dependence: while the index may produce false alarms during moderate anomalies, it becomes a highly reliable predictor for the most extreme, potentially disastrous precipitation events (e.g., strong El Niño years).

Furthermore, the λ_U for local evaporation and SST in 1+2 Niño region (not showed) remains consistently low (~ 0.5 and ~ 0.2, respectively) and does not increase for extreme quantiles. This lack of tail dependence provides further empirical evidence rejecting local moisture recycling as a driver of extremes, reinforcing the hypothesis that moisture convergence driven by dynamics is the dominant mechanism.

While ω_{500} serves as the superior diagnostic for instantaneous extremes, its utility for monitoring is limited by its chaotic nature. This was assessed through signal persistence analysis (Fig. 14). A rapid decorrelation was observed for ω_{500} (blue line), which loses significant memory after short lags. In contrast, ΔT (red line) exhibits high persistence, inheriting the thermal inertia of the SSTs. Crucially, the BWR (green line) demonstrates a predictability horizon significantly longer than that of pure ω_{500}. By integrating the thermodynamic component, the BWR effectively "anchors" the volatile dynamic signal to the slower-evolving boundary conditions. Thus, the BWR represents a physical trade-off: it sacrifices a marginal fraction of diagnostic precision at the extreme tail (compared to pure ω) to gain substantial signal stability and predictive memory, rendering it a more practical tool for sub-seasonal to seasonal monitoring.

5 Discussion

5.1 The Dynamic vs. Thermodynamic Control of Precipitation

The results obtained in this study provide robust empirical verification for the physical energy balance mechanism proposed by **?** for the tropical atmosphere. Through the application of Causal Discovery (PCMCI+) and Tail Dependence analysis, a clear hierarchy in the drivers of precipitation over the NWSA was established, distinguishing between the roles of thermodynamic potential and dynamic forcing.

It was demonstrated that while Sea Surface Temperature (SST) acts as a strong exogenous driver of parcel buoyancy (ΔT), as evidenced by the high causal strength in the PCMCI+ network, thermodynamic destabilization alone is insufficient to explain the variability of precipitation anomalies. The analysis of extremes revealed that ΔT exhibits asymptotic independence with respect to precipitation (Fig. A6), implying that extremely unstable environments do not linearly translate into extreme rainfall in the absence of a lifting mechanism. This limitation explains the "false positives" observed in purely thermodynamic indices (e.g., CAPE) over the Amazonian region (Fig. 3a-c), where high instability frequently coexists with convective inhibition.

Conversely, large-scale vertical motion (ω) was identified as the dominant control. The PCMCI+ analysis revealed that the causal effect of ω on precipitation is approximately three times stronger than that of local evaporation. Furthermore, ω was

the only variable to exhibit strong asymptotic dependence ($\lambda_U \approx 0.9$) during extreme events. Physically, this confirms that on climatic timescales, the release of latent heat (Q) in the NWSA is primarily balanced by adiabatic cooling associated with vertical ascent ($[\theta]_z\omega$), rather than by radiative cooling or local surface fluxes (**?**Lau et al., 1997).

The hypothesis that monthly precipitation anomalies are fueled significantly by local surface evaporation was critically challenged by the findings. The weak and physically secondary causal link observed between evaporation and precipitation, combined with the lack of tail dependence, suggests that the moisture sustaining deep convection is imported via dynamic moisture convergence rather than supplied by local recycling. This supports the notion that the NWSA operates under a "dynamically limited" regime rather than a "moisture limited" one.

This dynamic control explains the hydroclimatic decoupling observed during Central Pacific El Niño events, such as in 2016. Despite the presence of positive SST anomalies (Fig. A4j) and high thermodynamic potential, the precipitation response was neutralized by mid-tropospheric subsidence (Fig. 11j). Consequently, indices that rely solely on surface boundary conditions or thermodynamic profiles fail to capture the suppression of convection by the remote Walker circulation. By contrast, the dominant role of ω justifies the formulation of the BWR as an index that explicitly requires the coupling of the dynamic trigger with the thermodynamic fuel.

5.2 Advantages of BWR as a physical diagnostic proxy

Based on the hierarchy of physical drivers established in Sect. 4.2, the Buoyancy Work Rate (BWR) is proposed as a physical diagnostic proxy that integrates the essential components of the atmospheric energy cycle. While purely thermodynamic indices (e.g., CAPE) quantify the potential energy available and kinematic indices (e.g., ω) quantify the motion, the BWR represents the interaction between them.

A fundamental advantage of the BWR is its capacity to act as a physical filter for "regime mismatches." In the NWSA adjacent to the Niño 1+2 region, the atmosphere is directly influenced by the local eastern limb of the Walker circulation, characterized by a persistent subsidence branch that suppresses deep convection despite high surface thermodynamic potential. By mathematically coupling these terms (Eq. 1), the BWR yields near-zero values when high instability coexists with dynamic inhibition. This selectivity explains the superior diagnostic skill of the BWR in the coastal domain compared to purely thermodynamic predictors, which fail to capture the suppression of convection by the remote dynamic forcing of the Walker circulation.

It is acknowledged that the BWR, in its current formulation using pressure velocity (ω in Pa s^{-1}), does not possess strict units of power density (W m^{-2}). However, it functions as a proxy proportional to the rate of conversion of Available Potential Energy (APE) into Kinetic Energy (KE) within the atmospheric column. This formulation is physically grounded in the framework of **?**, where the generation of kinetic energy maintains the circulation against dissipation. Therefore, the BWR provides a more direct measure of the intensity of the "atmospheric heat engine" driving regional variability than precipitation anomalies alone, which are influenced by local moisture recycling and microphysical efficiency.

From a monitoring perspective, the hybrid nature of the index offers a significant advantage over the use of pure vertical velocity. Although ω was identified as the primary control for precipitation extremes (Sect. 4.4), its signal is inherently chaotic

and exhibits rapid decorrelation, limiting its utility for sub-seasonal monitoring. The autocorrelation analysis demonstrated that the inclusion of the thermodynamic component (ΔT) effectively transfers the thermal inertia of the ocean boundary conditions (SST) to the index. This confers a "thermal memory" to the BWR, resulting in a signal that remains physically consistent with the dynamic control required by the **?** mechanism, yet is sufficiently stable on monthly timescales to be utilized in early warning applications.

5.3 Physical limitations and interpretation of errors

Despite the robust performance of the BWR during extreme events, significant limitations exist in moderate regimes, as evidenced by the dispersion observed in the copula space (Sect. 4.4). A primary limitation of the BWR formulation is the exclusion of an explicit humidity term and an entrainment parameter. The index assumes that the product $-\omega\Delta T$ is proportional to the generation of kinetic energy and subsequent rainfall. However, this holds strictly true only in environments where the moisture supply is sufficient to reach saturation and release latent heat (Q).

In cases of "dry ascent," where strong dynamic lifting occurs in a moisture-starved environment, the BWR may yield high positive values that do not translate into precipitation. This physical decoupling likely explains the false positives observed in the lower-right quadrant of the dependence plot. This limitation is consistent with the energy balance of **?**, where the term Q is assumed to be balanced by adiabatic cooling ($[\theta]_z\omega$). If the air is too dry, Q is limited by moisture availability rather than vertical motion. Consequently, the BWR measures the intensity of the circulation's "engine" but not necessarily the efficiency of its output.

Furthermore, "false negatives" (low BWR, high precipitation) were observed, particularly along the eastern slopes of the Andes and in transition zones. These discrepancies are attributable to two factors. First, the BWR is integrated from the surface to 100 hPa to isolate deep convection; therefore, precipitation driven by shallow convection or warm rain processes—which do not involve deep tropospheric ascent—is systematically underestimated. Second, precipitation driven by mechanical orographic lifting can occur under conditions of weak large-scale ω or moderate instability, mechanisms that are not fully resolved at the resolution of the reanalysis data.

Finally, it must be reiterated that the BWR is a climatic diagnostic proxy and not a direct measure of precipitation physics. Unlike complex convective parameterization schemes, the BWR was designed to monitor the macroscopic state of the local branch of the Walker circulation between Peru and Ecuador. The Tail Dependence analysis confirms that while these limitations introduce noise during moderate conditions, the influence of dry entrainment and shallow processes becomes secondary during extreme El Niño events. In such regimes, the massive moisture supply and intense dynamic forcing render the BWR a highly reliable indicator for disaster risk management.

Code and data availability. PISCO V2.1 dataset is available at https://iridl.ldeo.columbia.edu/SOURCES/.SENAMHI/.HSR/.PISCO/index.html; RAIN4PE at https://datapub.gfz-potsdam.de/download/10.5880.PIK.2020.010enouiv/; ERA5 reanalysis data at https://cds.climate.copernicus.eu/datasets

Author contributions. All authors designed the study, analyzed and interpreted the results, and wrote and reviewed the manuscript.

Competing interests. The authors declare no competing interests.

Acknowledgements. The authors extend their gratitude to Ricardo Gutierrez for his support with recommendations and suggestions and to Ken Takahashi for recommending articles to discuss the physical basis.

References

Adachi, N., Takemura, K., Sato, H., and Kamiguchi, K.: A case study of coastal El Niño event in early 2017, in: 98th American Meteorological Society Annual Meeting, https://ams.confex.com/ams/98Annual/webprogram/Paper333553.html, 2018.

Aguirre-Correa, F., Bollasina, M., Garreaud, R., and Suárez, F.: Rossby waves as key drivers of the South American Monsoon high-frequency variability, Atmospheric Research, 326, 108 206, https://doi.org/10.1016/j.atmosres.2025.108206, 2025.

Aliaga-Nestares, V., Rodriguez-Zimmermann, D., and Quispe-Gutiérrez, N.: Behavior of the ITCZ second band near the Peruvian coast during the 2017 coastal El Niño, Atmósfera, 36, 23–39, https://doi.org/10.20937/ATM.53063, 2023.

Aybar, C., Fernández, C., Huerta, A., Lavado, W., Vega, F., and Felipe-Obando, O.: Construction of a high-resolution gridded rainfall dataset for Peru from 1981 to the present day, Hydrological Sciences Journal, 65, 770–785, https://doi.org/10.1080/02626667.2019.1649411, 2019.

Bolton, D.: The Computation of Equivalent Potential Temperature, Monthly Weather Review, 108, 1046–1053, https://doi.org/10.1175/1520-0493(1980)108<1046:tcoept>2.0.co;2, 1980.

Bony, S., Lau, K.-M., and Sud, Y. C.: Sea Surface Temperature and Large-Scale Circulation Influences on Tropical Greenhouse Effect and Cloud Radiative Forcing, Journal of Climate, 10, 2055–2077, https://doi.org/10.1175/1520-0442(1997)010<2055:sstals>2.0.co;2, 1997.

Callahan, C. W. and Mankin, J. S.: Persistent effect of El Niño on global economic growth, Science, 380, 1064–1069, https://doi.org/10.1126/science.adf2983, 2023.

Cornejo-Garrido, A. G. and Stone, P. H.: On the heat balance of the Walker circulation, Journal of the Atmospheric Sciences, 34, 1155–1162, https://doi.org/10.1175/1520-0469(1977)034<1155:OTHBOT>2.0.CO;2, 1977.

DeMott, C. A. and Randall, D. A.: Observed variations of tropical convective available potential energy, Journal of Geophysical Research: Atmospheres, 109, https://doi.org/10.1029/2003jd003784, 2004.

Echevin, V., Colas, F., Espinoza-Morriberon, D., Vasquez, L., Anculle, T., and Gutierrez, D.: Forcings and Evolution of the 2017 Coastal El Niño Off Northern Peru and Ecuador, Frontiers in Marine Science, 5, https://doi.org/10.3389/fmars.2018.00367, 2018.

Emanuel, K. A.: Atmospheric convection, Oxford University Press, ISBN 9780195066302, 1994.

Fernandez-Palomino, C. A., Hattermann, F. F., Krysanova, V., Lobanova, A., Vega-Jácome, F., Lavado, W., Santini, W., Aybar, C., and Bronstert, A.: A novel high-resolution gridded precipitation dataset for Peruvian and Ecuadorian watersheds: Development and hydrological evaluation, Journal of Hydrometeorology, 23, 309–336, https://doi.org/10.1175/JHM-D-20-0285.1, 2022.

Garreaud, R. D.: A plausible atmospheric trigger for the 2017 coastal El Niño, International Journal of Climatology, 38, https://doi.org/10.1002/joc.5426, 2018.

Gálvez, J. M.: The Gálvez-Davison Index (GDI), Weather Prediction Center, National Oceanic and Atmospheric Administration, https://www.wpc.ncep.noaa.gov/international/gdi/, 2016.

Han, Y., Zhang, M.-Z., Xu, Z., and Guo, W.: Assessing the performance of 33 CMIP6 models in simulating the large-scale environmental fields of tropical cyclones, Climate Dynamics, 58, 1683–1698, https://doi.org/10.1007/s00382-021-05986-4, 2022.

Hersbach, H., Bell, B., Berrisford, P., Hirahara, S., Horányi, A., Muñoz-Sabater, J., Nicolas, J., Peubey, C., Radu, R., Schepers, D., Simmons, A., Soci, C., Abdalla, S., Abellan, X., Balsamo, G., Bechtold, P., Biavati, G., Bidlot, J., Bonavita, M., De Chiara, G., Dahlgren, P., Dee, D., Diamantakis, M., Dragani, R., Flemming, J., Forbes, R., Fuentes, M., Geer, A., Haimberger, L., Healy, S., Hogan, R. J., Hólm, E., Janisková, M., Keeley, S., Laloyaux, P., Lopez, P., Lupu, C., Radnoti, G., de Rosnay, P., Rozum, I., Vamborg, F., Villaume, S., and Thépaut,

J.: The ERA5 global reanalysis, Quarterly Journal of the Royal Meteorological Society, 146, 1999–2049, https://doi.org/10.1002/qj.3803, 2020.

Houze, R. A.: Mesoscale convective systems, Reviews of Geophysics, 42, https://doi.org/10.1029/2004rg000150, 2004.

Imfeld, N., Sedlmeier, K., Gubler, S., Correa Marrou, K., Davila, C. P., Huerta, A., Lavado-Casimiro, W., Rohrer, M., Scherrer, S. C., and Schwierz, C.: A combined view on precipitation and temperature climatology and trends in the southern Andes of Peru, International Journal of Climatology, 41, 679–698, https://doi.org/10.1002/joc.6645, 2021.

John, V. and Soden, B.: Temperature and humidity biases in global climate models and their impact on climate feedbacks, Geophysical Research Letters, 34, https://doi.org/10.1029/2007GL030429, 2007.

Lau, K.-M., Wu, H.-T., and Bony, S.: The Role of Large-Scale Atmospheric Circulation in the Relationship between Tropical Convection and Sea Surface Temperature, Journal of Climate, 10, 381–392, https://doi.org/10.1175/1520-0442(1997)010<0381:trolsa>2.0.co;2, 1997.

Lavado-Casimiro, W. S., Felipe, O., Silvestre, E., and Bourrel, L.: ENSO impact on hydrology in Peru, Advances in Geosciences, 33, 33–39, https://doi.org/10.5194/adgeo-33-33-2013, 2013.

McPhaden, M. J., Zebiak, S. E., and Glantz, M. H.: ENSO as an Integrating Concept in Earth Science, Science, 314, 1740–1745, https://doi.org/10.1126/science.1132588, 2006.

Nelsen, R. B.: An introduction to copulas, Springer, https://doi.org/10.1007/0-387-28678-0, 2006.

Paek, H., Yu, J., and Qian, C.: Why were the 2015/2016 and 1997/1998 extreme El Niños different?, Geophysical Research Letters, 44, 1848–1856, https://doi.org/10.1002/2016gl071515, 2017.

Peng, Q., Xie, S.-P., Passalacqua, G. A., Miyamoto, A., and Deser, C.: The 2023 extreme coastal El Niño: Atmospheric and air-sea coupling mechanisms, Science Advances, 10, https://doi.org/10.1126/sciadv.adk8646, 2024.

Poulin, A., Huard, D., Favre, A.-C., and Pugin, S.: Importance of tail dependence in bivariate frequency analysis, Journal of Hydrologic Engineering, 12, 394–403, https://doi.org/10.1061/(ASCE)1084-0699(2007)12:4(394), 2007.

Poveda, G., Waylen, P. R., and Pulwarty, R. S.: Annual and inter-annual variability of the present climate in northern South America and southern Mesoamerica, Palaeogeography, Palaeoclimatology, Palaeoecology, 234, 3–27, https://doi.org/10.1016/j.palaeo.2005.10.031, 2006.

Poveda, G., Mejia, J. F., Arias, P. A., Zuluaga, M. D., Salazar, J. F., Carmona, A. M., Builes-Jaramillo, A., Salas, H. D., Yepes, J., Martinez, J. A., and Bedoya-Soto, J. M.: Climate of Northwestern South America, https://doi.org/10.1093/acrefore/9780190228620.013.966, 2025.

Rivas Quispe, P. R., Anderson-Frey, A., and Mcmurdie, L. A.: An index for precipitation on the north coast of Peru using logistic regression, Atmósfera, 38, 55–73, https://doi.org/10.20937/ATM.53232, 2024.

Rodríguez-Morata, C., Díaz, H. F., Ballesteros-Canovas, J. A., Rohrer, M., and Stoffel, M.: The anomalous 2017 coastal El Niño event in Peru, Climate Dynamics, 52, 5605–5622, https://doi.org/10.1007/s00382-018-4466-y, 2018.

Rudloff, D., Lübbecke, J. F., and Wahl, S.: Seasonality of feedback mechanisms involved in Pacific coastal Niño events, Climate Dynamics, 63, 58, https://doi.org/10.1007/s00382-024-07131-y, 2025.

Runge, J.: Discovering contemporaneous and lagged causal relations in autocorrelated nonlinear time series datasets, in: Proceedings of the 36th Conference on Uncertainty in Artificial Intelligence (UAI), pp. 1388–1397, PMLR, http://proceedings.mlr.press/v124/runge20a.html, 2020.

Sanabria, J., Carrillo, C. M., and Labat, D.: Unprecedented Rainfall and Moisture Patterns during El Niño 2016 in the Eastern Pacific and Tropical Andes: Northern Perú and Ecuador, Atmosphere, 10, 768, https://doi.org/10.3390/atmos10120768, 2019.

Sulca, J.: Evidence of nonlinear Walker circulation feedbacks on extreme El Niño Pacific diversity: Observations and CMIP5 models, International Journal of Climatology, 41, 2934–2961, https://doi.org/10.1002/joc.6998, 2021.

Sulca, J. and Takahashi, K.: Forecasting austral summer precipitation along the western coast of South America (WCSA), Environmental Research Communications, 7, 101 005, https://doi.org/10.1088/2515-7620/ae0de9, 2025.

Sulca, J., Takahashi, K., Espinoza, J., Vuille, M., and Lavado-Casimiro, W.: Impacts of different<scp>ENSO</scp>flavors and tropical Pacific convection variability (<scp>ITCZ</scp>,<scp>SPCZ</scp>) on austral summer rainfall in South America, with a focus on Peru, International Journal of Climatology, 38, 420–435, https://doi.org/10.1002/joc.5185, 2017.

Takahashi, K.: The atmospheric circulation associated with extreme rainfall events in Piura, Peru, during the 1997–1998 and 2002 El Niño events, Annales Geophysicae, 22, 3917–3926, https://doi.org/10.5194/angeo-22-3917-2004, 2004.

Takahashi, K. and Dewitte, B.: Strong and moderate nonlinear El Niño regimes, Climate Dynamics, 46, 1627–1645, https://doi.org/10.1007/s00382-015-2665-3, 2016.

Takahashi, K. and Martínez, A. G.: The very strong coastal El Niño in 1925 in the far-eastern Pacific, Climate Dynamics, 52, 7389–7415, https://doi.org/10.1007/s00382-017-3702-1, 2017.

Takahashi, K., Montecinos, A., Goubanova, K., and Dewitte, B.: ENSO regimes: Reinterpreting the canonical and Modoki El Niño, Geophysical Research Letters, 38, https://doi.org/10.1029/2011GL047364, 2011.

Takahashi, K., Aliaga-Nestares, V., Avalos, G., Bouchon, M., Castro, A., Cruzado, L., Dewitte, B., Gutiérrez, D., Lavado-Casimiro, W., Marengo, J., et al.: The 2017 coastal El Niño, Bulletin of the American Meteorological Society, 99, S210–S211, https://doi.org/10.1175/2018BAMSStateoftheClimate.1, 2018.

Thielen, D. R., Ramoni-Perazzi, P., Zamora-Ledezma, E., Puche, M. L., Marquez, M., Quintero, J. I., Rojas, W., Quintero, A., Bianchi, G., Soto-Werschitz, I. A., and Arizapana-Almonacid, M. A.: Effect of extreme El Niño events on the precipitation of Ecuador, Natural Hazards and Earth System Sciences, 23, 1507–1527, https://doi.org/10.5194/nhess-23-1507-2023, 2023.

Trenberth, K. E.: The definition of El Niño, Bulletin of the American Meteorological Society, 78, 2771–2778, https://doi.org/10.1175/1520-0477(1997)078<2771:TDOEN>2.0.CO;2, 1997.

Wang, C., Deser, C., Yu, J.-Y., DiNezio, P., and Clement, A.: El Niño and Southern Oscillation (ENSO): A Review, p. 85–106, Springer Netherlands, ISBN 9789401774994, https://doi.org/10.1007/978-94-017-7499-4_4, 2016.

Williams, E. and Renno, N.: An Analysis of the Conditional Instability of the Tropical Atmosphere, Monthly Weather Review, 121, 21–36, https://doi.org/10.1175/1520-0493(1993)121<0021:aaotci>2.0.co;2, 1993.

Yu, H. and Zhang, M.: Explaining the year-to-year variability of the Eastern Pacific intertropical convergence zone in the boreal spring, Journal of Geophysical Research: Atmospheres, 123, 3847–3856, https://doi.org/10.1002/2017JD028168, 2018.

Zipser, E. J.: Some Views On “Hot Towers” after 50 Years of Tropical Field Programs and Two Years of TRMM Data, Meteorological Monographs, 29, 49–49, https://doi.org/10.1175/0065-9401(2003)029<0049:csvoht>2.0.co;2, 2003.

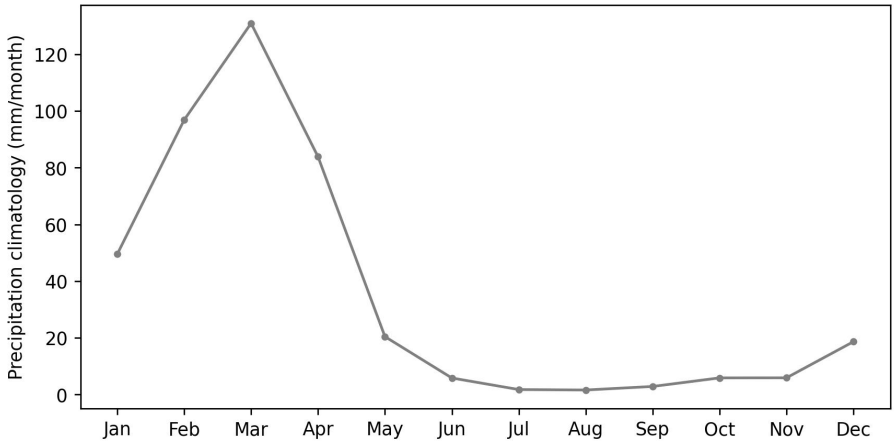

Figure 1. Precipitation climatology as the 1981–2015 median from ERA5 averaged over the NWSA next to 1+2 El Niño region.

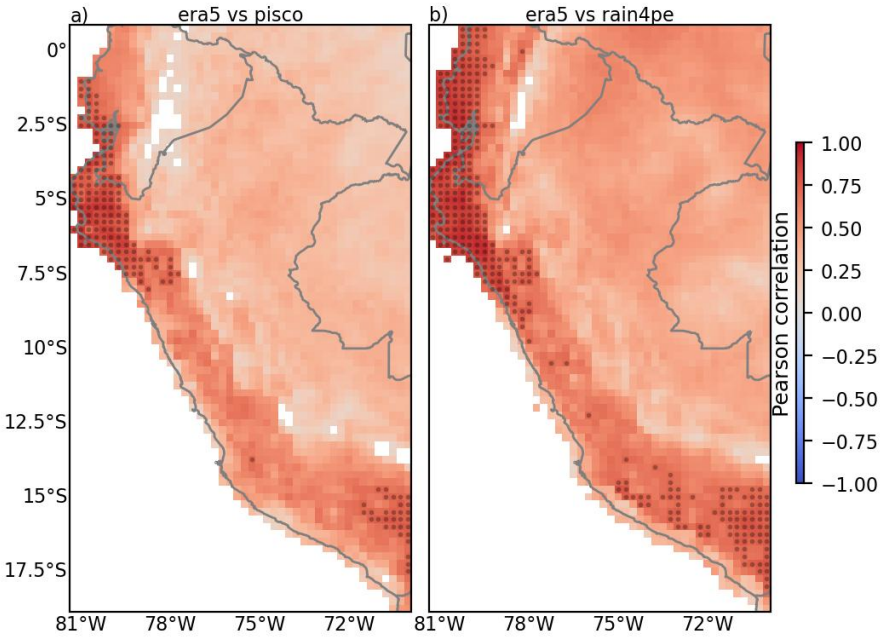

Figure 2. Pearson correlation (R) at the 95% confidence level between monthly precipitation anomaly from ERA5 and PISCO (a) for 1981–2025, and RAIN4PE (b) for 1981–2015. Only pixels with significant R (p-value<0.05) are shown, the gray points represent R>0.7. The blue (red) shaded colors indicate negative (positive) values of R. Anomalies were calculated taking the 1981–2015 median as climatology.

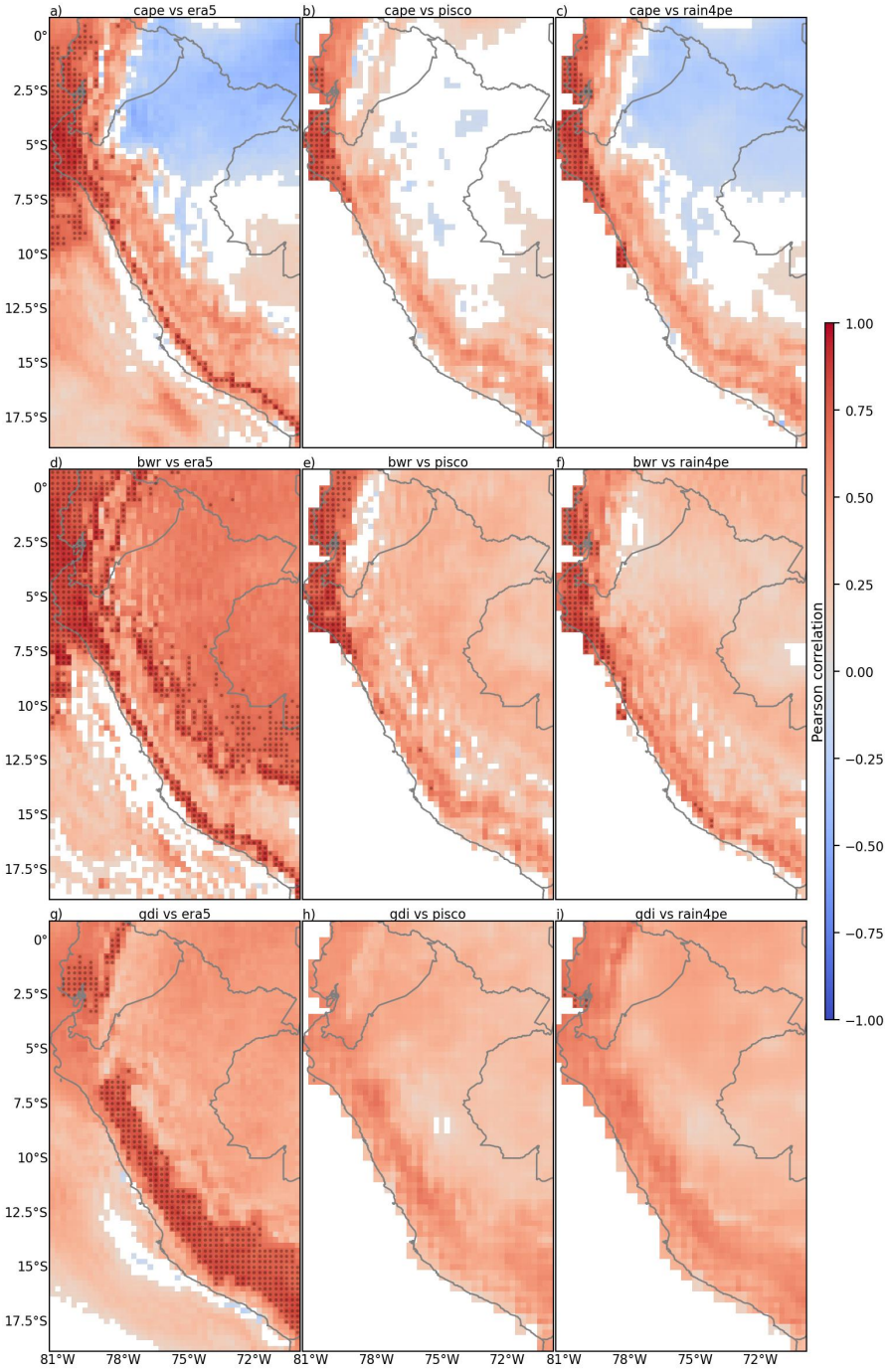

Figure 3. Pearson correlation (R) maps at the 95% confidence level between monthly anomalies of convective indices (rows) and precipitation datasets (columns) for the 1981–2015 common period. The indices (rows) are (a-c) CAPE, (d-f) BWR, (g-i) GDI, (h-l) Ia, and (m-o) Id. The precipitation datasets (columns) are (a, d, g) ERA5, (b, e, h) PISCO, and (c, f, i) RAIN4PE. Shading is shown only for significant correlations (p-value < 0.05). Red (blue) indicates positive (negative) R values. Gray points highlight strong correlations (R > 0.7). Anomalies were calculated taking the 1981–2015 median as climatology.

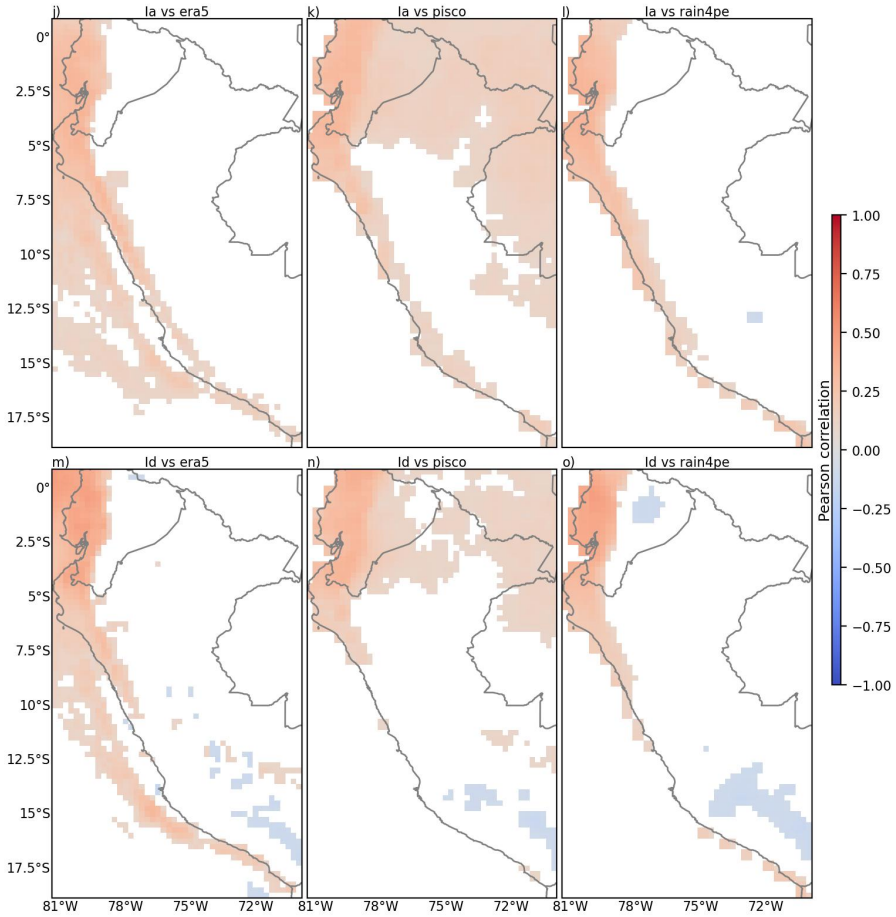

Figure 3. (Continued).

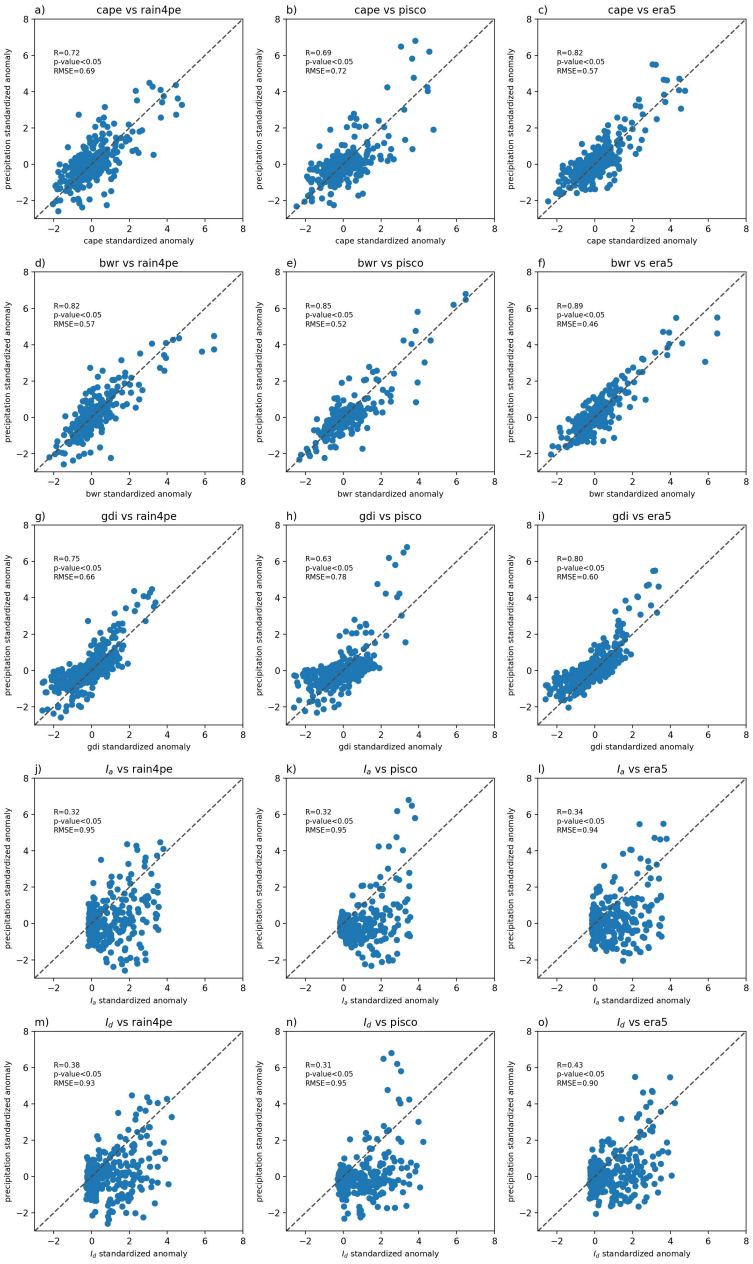

Figure 4. Scatterplots between convective indices and precipitation datasets over the NWSA adjacent to Niño 1+2. Scatterplots comparing monthly standardized anomalies of CAPE (a-c), BWR (d-f), GDI (g-i), (h-l) Ia, and (m-o) Id against standardized precipitation anomalies from ERA5 (left column), PISCO (middle column), and RAIN4PE (right column). All data are spatially averaged over the NWSA adjacent to Niño 1+2. The Pearson correlation coefficient (R), RMSE and the significance at the 95% confidence level (p-value < 0.05) are shown in each panel. The diagonal dashed line is the identity function.

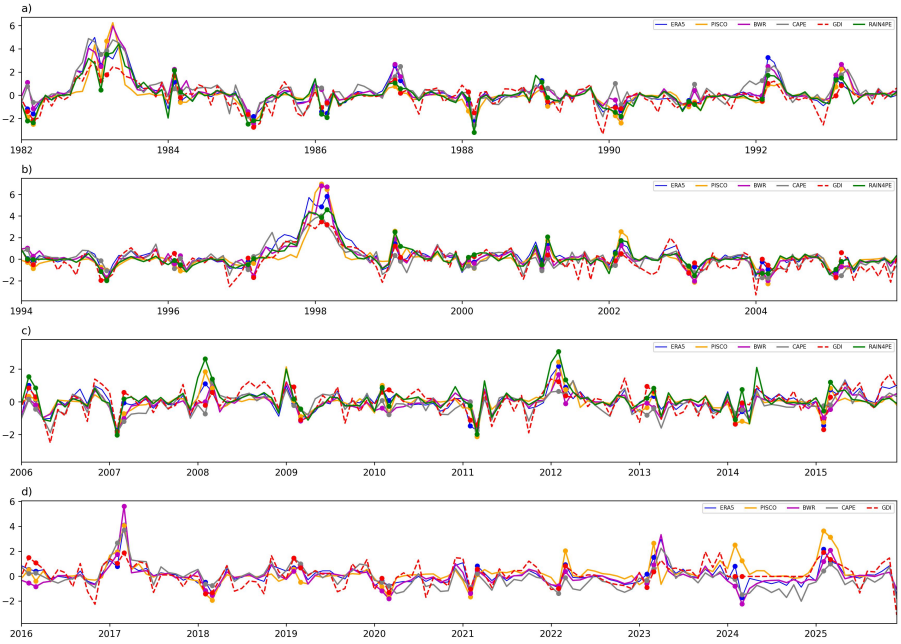

Figure 5. Time series of monthly standardized anomalies of convective indices, such as CAPE (gray), BWR (magenta), and GDI (dashed red), and standardized precipitation from ERA5 (blue), PISCO (orange), and RAIN4PE (green). All data are spatially averaged over the NWSA adjacent to Niño 1+2 for the period 1981–2025. The RAIN4PE dataset is only available for 1981–2015. Anomalies were calculated taking the 1981–2015 median as climatology. Circle markers indicate February and March of every year.

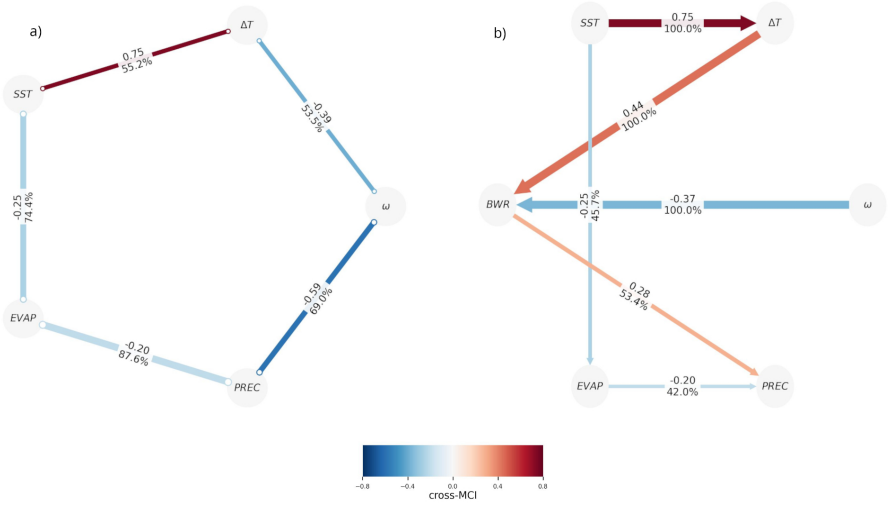

Figure 6. Causal graphs without BWR (a) and with BWR (b). Red (blue) colors indicate direct (inverse) relationship. Arrows indicate the causal directions. Labels in middle of arrows indicate MCI values and confidence of the 5000 bootstrap samples. All variables were averaged over (81.25° W–78.5° W, 8° S–0.75° N), except SST, which was averaged over Niño 1+2 region.

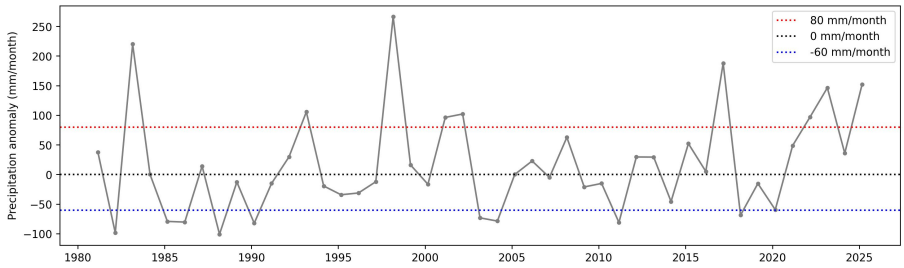

Figure 7. Monthly precipitation anomaly time series in March from PISCO, taking the 1981–2015 median as climatology, averaged over the NWSA next to 1+2 El Niño region. Points above (below) horizontal red (blue) dotted line are considered as rainiest (driest) events.

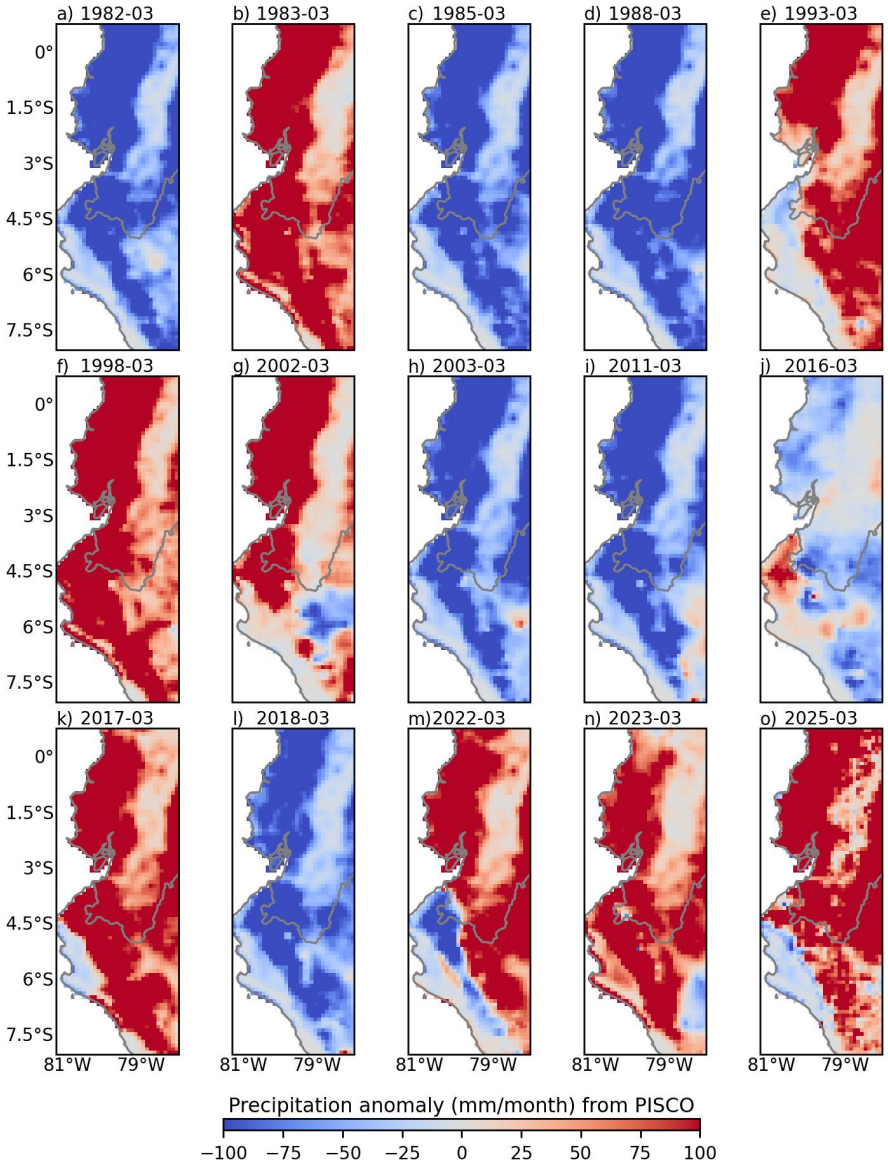

Figure 8. Precipitation anomaly distribution, taking the 1981–2015 median as climatology, from PISCO for the rainiest and driest events identified in Sect. 4. The blue (red) shaded colors indicate negative (positive) values of precipitation.

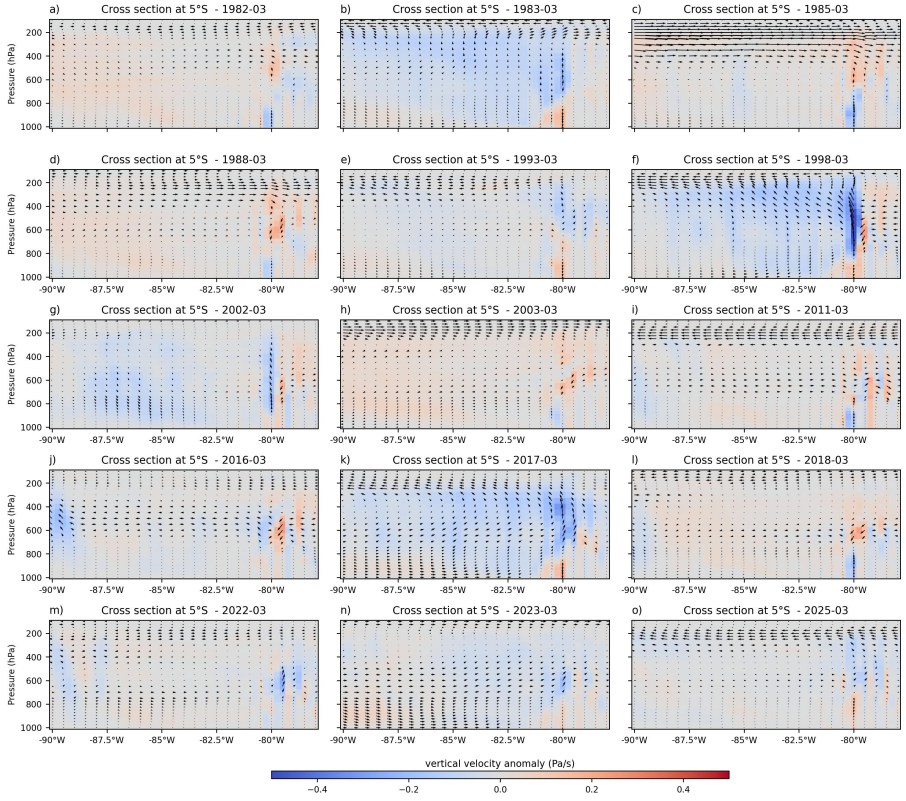

Figure 9. Longitudinal cross-section of the resultant vector between the anomalies of ω and zonal wind at 5° S for the rainiest and driest events identified in Sect. 4. The blue (red) shaded colors indicate negative (positive) values of ω. The ω vector was multiplied by -20 to increase its scale and to get upward (downward) arrows with the air ascent (descent). Anomalies were calculated taking the 1981–2015 median as climatology.

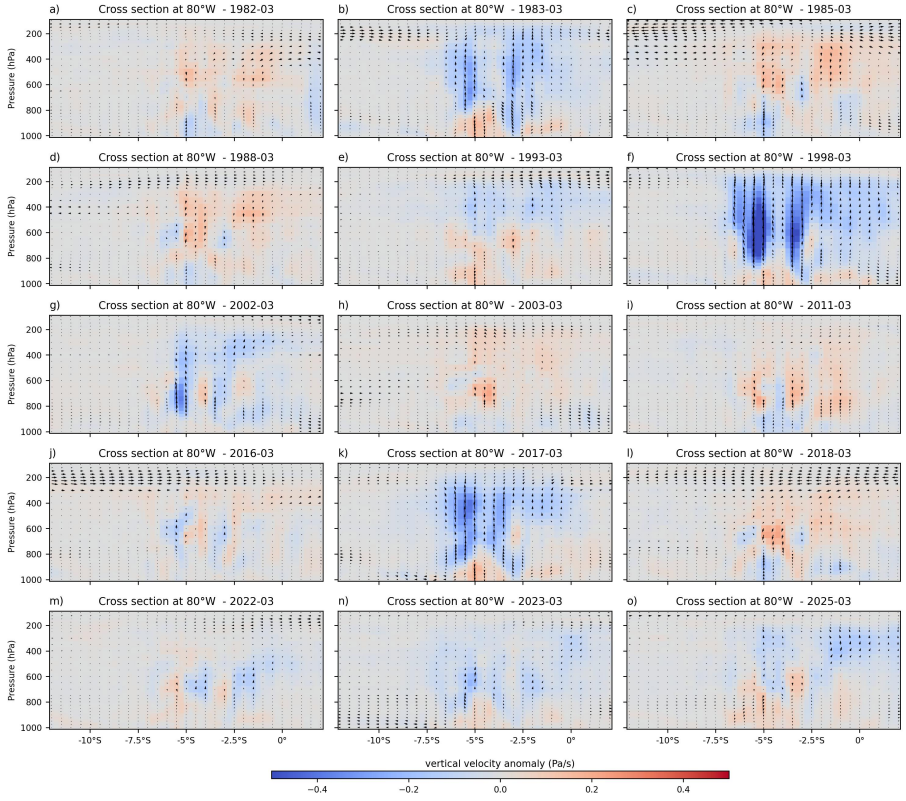

Figure 10. Latitudinal cross-section of the resultant vector between the anomalies of ω and meridional wind at 80° W for the rainiest and driest events identified in Sect. 4. The blue (red) shaded colors indicate negative (positive) values of ω. The ω vector was multiplied by -20 to increase its scale and to get upward (downward) arrows with the air ascent (descent). Anomalies were calculated taking the 1981–2015 median as climatology.

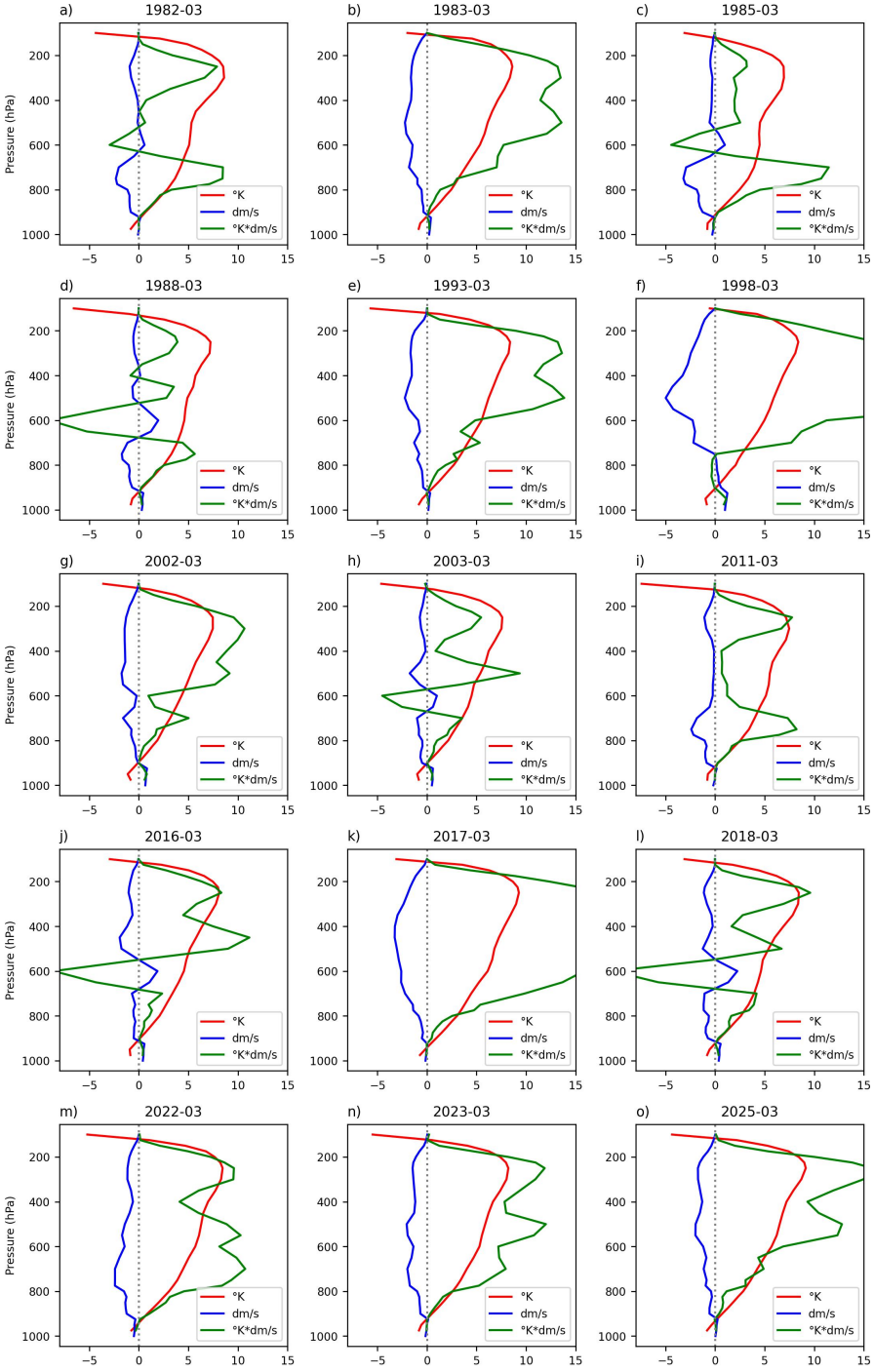

Figure 11. Profiles of ΔT (red), ω (blue) and $-\omega\Delta T$ (green) at (80° W,5° S) for the rainiest and driest events identified in Sect. 4. The LCL, LFC and EL dotted horizontal lines represent the lifting condensation level, the level of free convection and the equilibrium level respectively. The ω was multiplied by 10 to increase its scale.

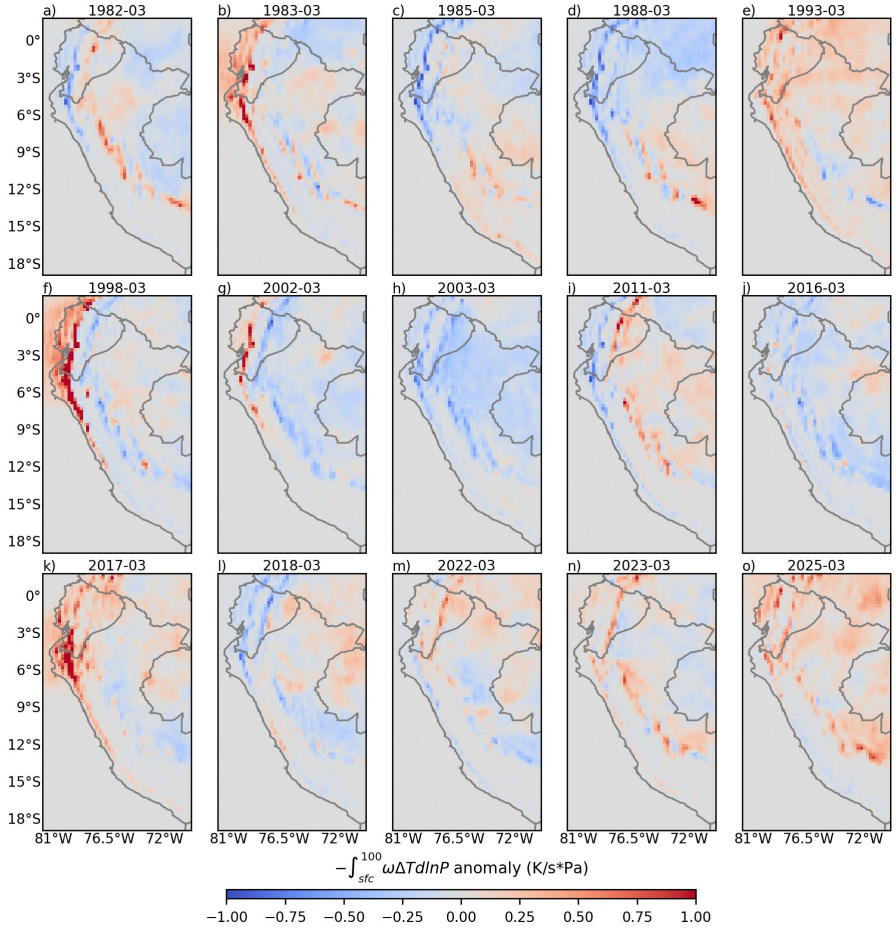

Figure 12. BWR anomaly, taking the 1981–2015 median as climatology, for the rainiest and driest events identified in Sect. 4. The blue (red) shaded colors indicate negative (positive) values of BWR. Positive (negative) values indicate favorable (unfavorable) conditions for deep convection.

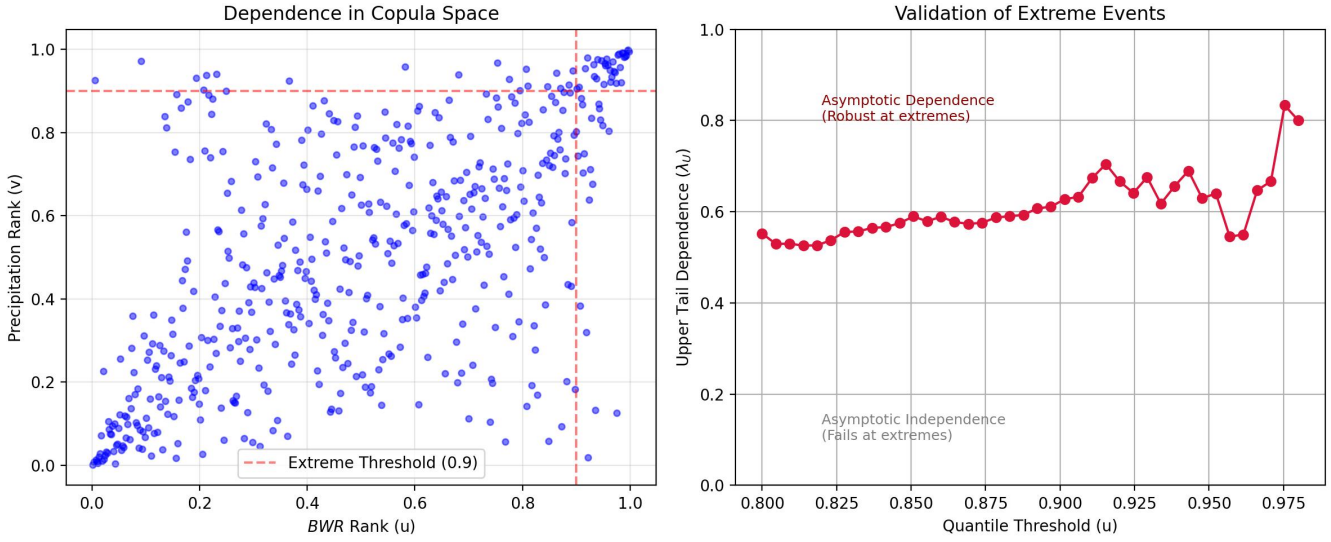

Figure 13. Analysis of the extreme dependence structure between BWR index and precipitation anomalies in the NWSA adjacent to Niño 1+2. **(a)** Scatterplot of pseudo-observations (uniform ranks) in the empirical copula space. The dashed red lines indicate the 0.90 quantile threshold; points in the upper-right quadrant represent concurrent extreme events. **(b)** The empirical Upper Tail Dependence Coefficient (λ_U) as a function of the quantile threshold (u).

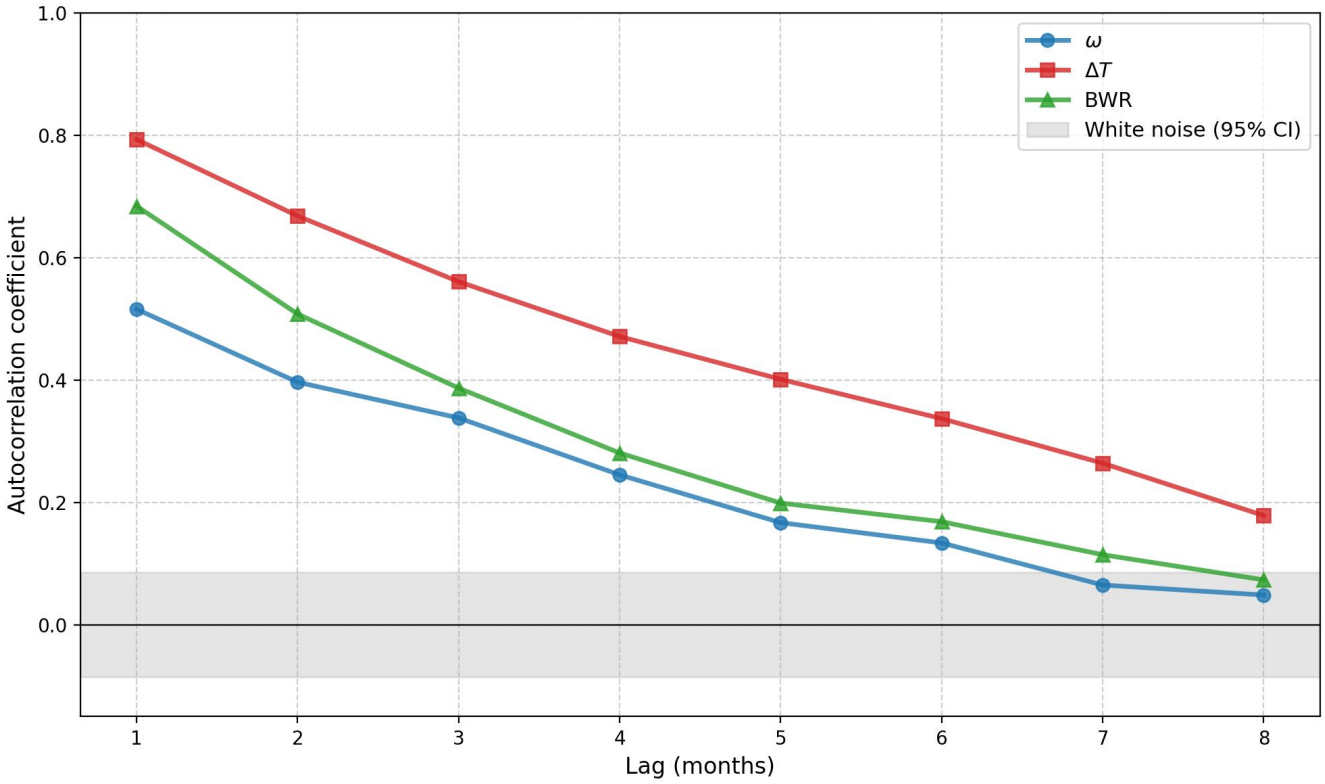

Figure 14. Analysis of signal persistence and predictability horizons for the physical components of the BWR index. The plot displays the autocorrelation function (ACF) for vertical velocity (ω, blue), parcel buoyancy 400-700 hPa average (ΔT, red), and the BWR index (green) up to a lag of 8 months. The gray shaded area indicates the 95% confidence interval for a white noise process ($\pm 1.96/\sqrt{N}$).

Appendix A

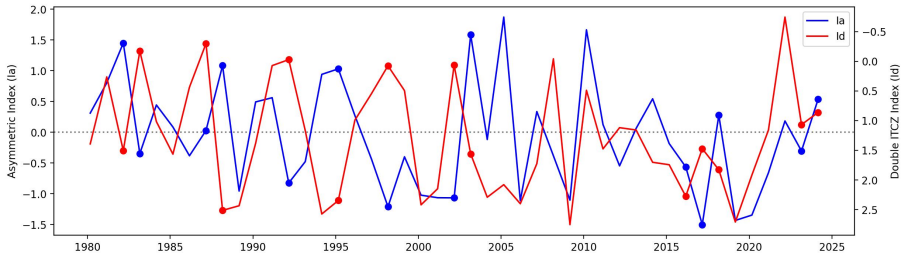

Figure A1. Time series of the March Ia and Id indices for the period 1981–2025 taking the same areas proposed by Aliaga-Nestares et al. (2023).

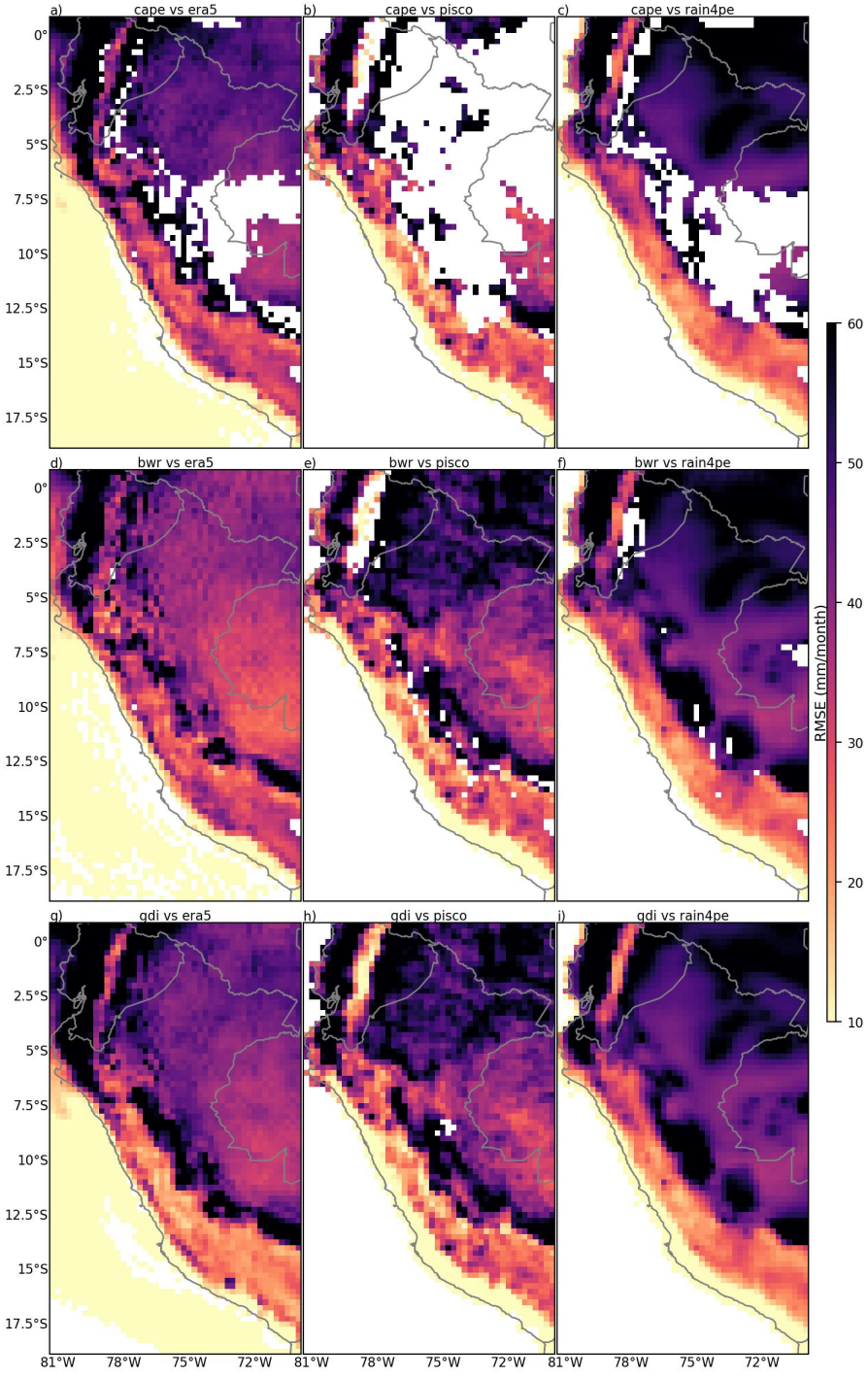

Figure A2. Spatial distribution of RMSE in mm month^{-1} for the common period 1981–2015. Anomaly precipitation was estimated using linear regression based on five convective indices: CAPE (a-c), BWR (d-f), GDI (g-i), (h-l) Ia, and (m-o) Id. The RMSE was calculated by comparing the estimates against three precipitation anomaly products: ERA5 (left column), PISCO (middle column), and RAIN4PE (right column). Values are only displayed for pixels with a significant regression ($p < 0.05$).

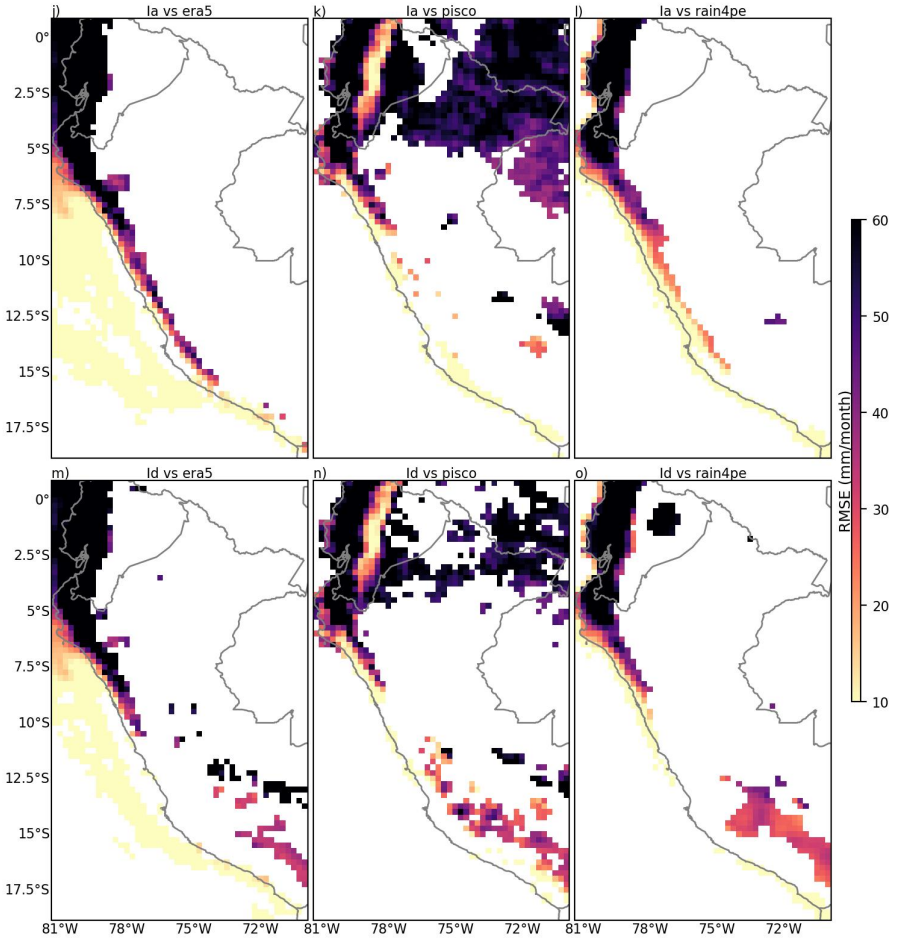

Figure A2. (Continued).

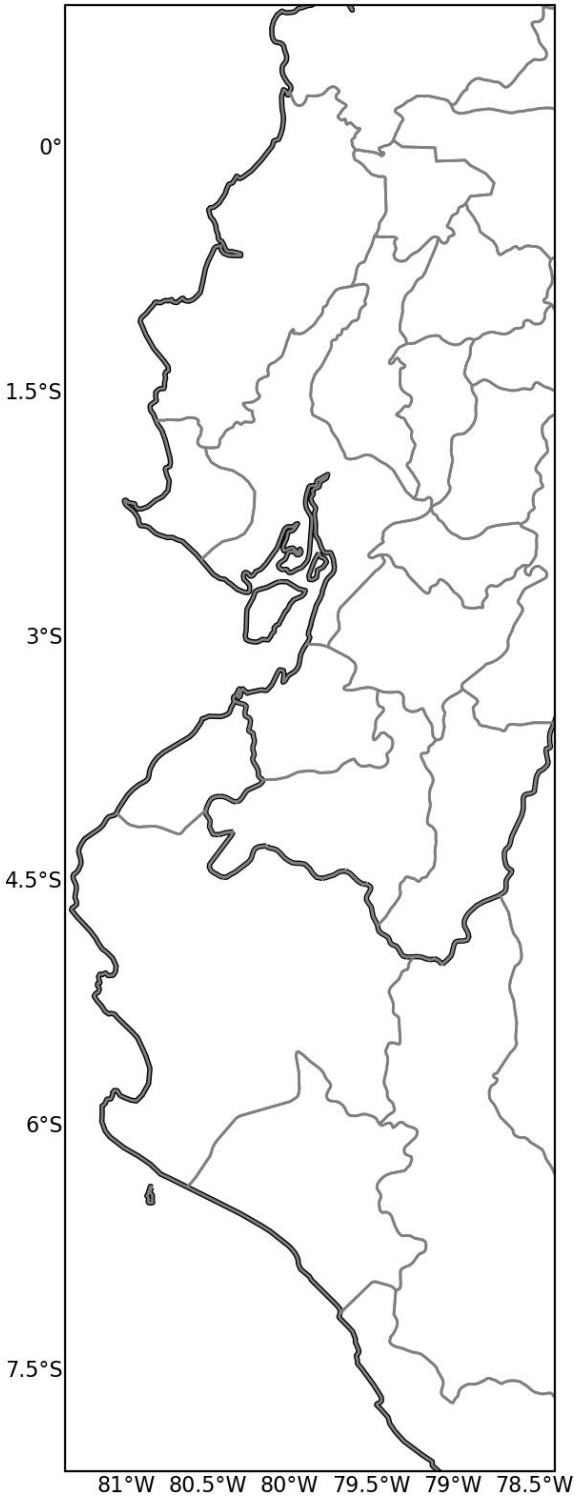

Figure A3. NWSA adjacent to Niño 1+2 area (81.25° W–78.5° W, 8° S–0.75° N).

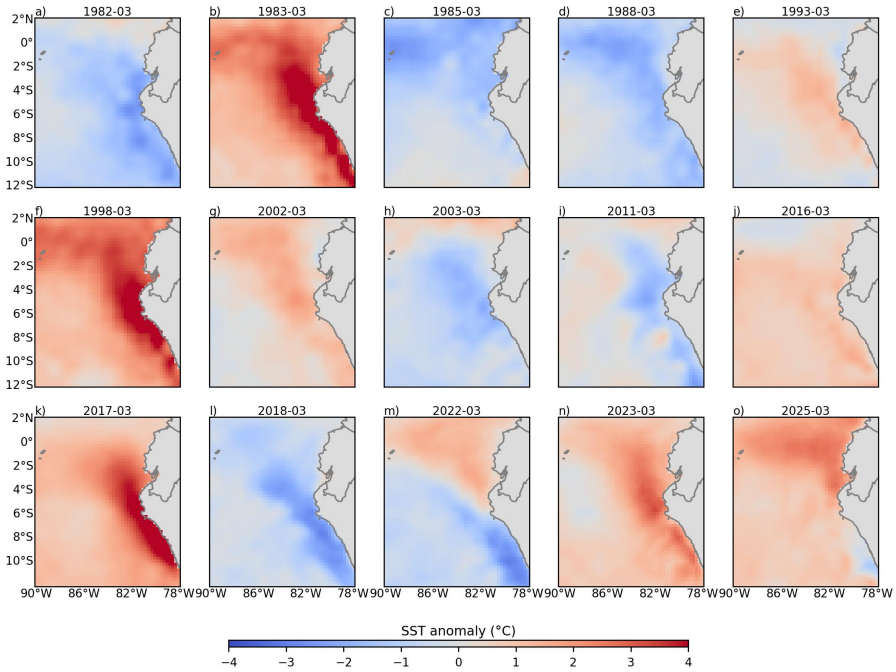

Figure A4. SST anomaly from ERA5 for the rainiest and driest events identified in Sect. 4 over the Niño 1+2 region. The blue (red) shaded colors indicate negative (positive) values of SST.

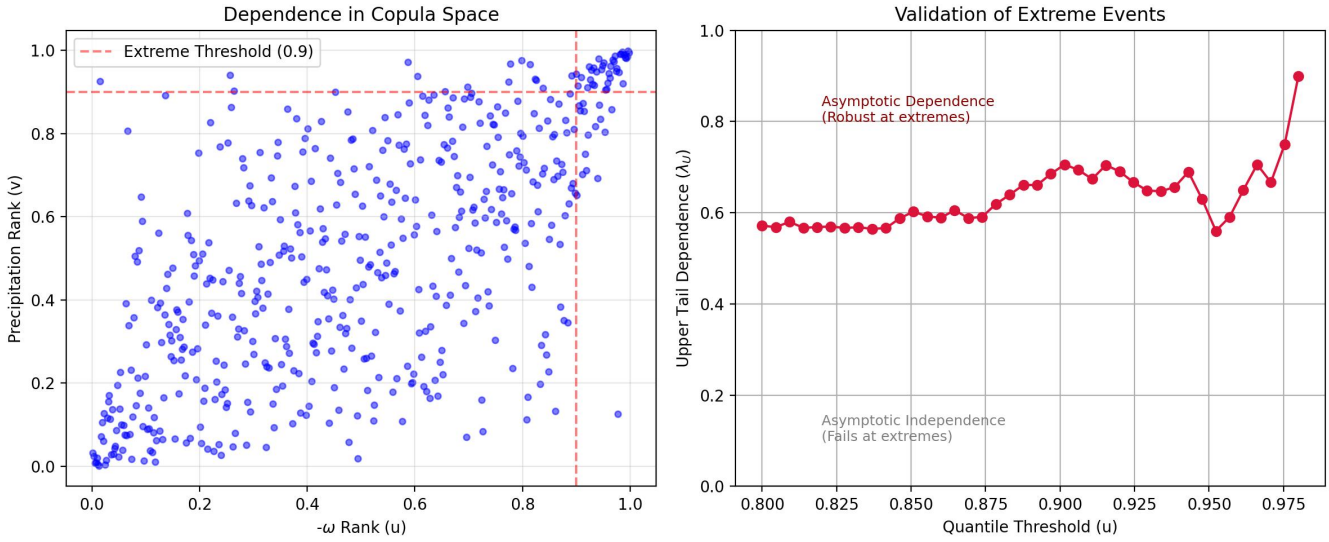

Figure A5. Same as Fig. 13, but for the ω at 500 hPa.

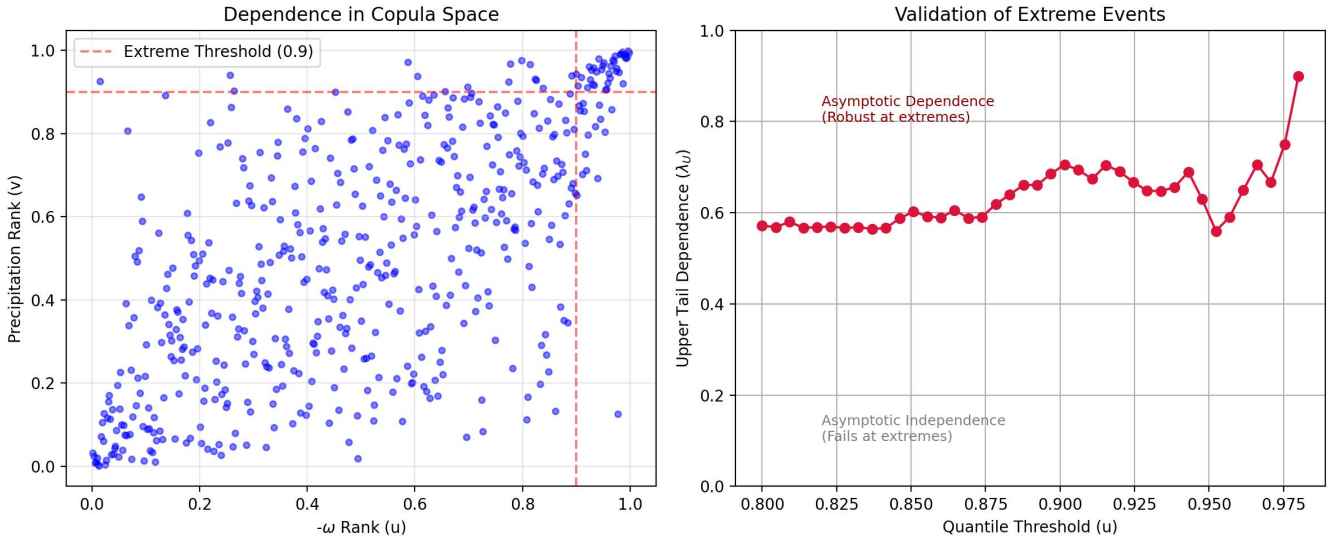

Figure A6. Same as Fig. 13, but for the 400–700 hPa ΔT.